The Meteoritical Society

Meteoritics & Planetary Science 53, Nr 6, 1179–1206 (2018)
doi: 10.1111/maps.13065

Hapke mixture modeling applied to VNIR spectra of mafic mineral mixtures and shergottites: Implications for quantitative analysis of satellite data

Jennifer K. HARRIS* and Peter M. GRINDROD

Earth Sciences, Natural History Museum, Cromwell Road, Kensington, London SW7 5BD, UK
*Corresponding author. E-mail: jennifer.harris@ucl.ac.uk

(Received 21 September 2017; revision accepted 31 January 2018)

Abstract–The mineralogy of Mars is well understood on a qualitative level at a global scale due to satellite data. Quantitative analysis of visible and near-infrared (VNIR) satellite data is a desirable but nontrivial task, due partly to the nonlinearity of VNIR reflectance spectra from the mineral mixtures of the Martian surface. In this study, we investigated the use of the Hapke radiative transfer model to generate linearly mixed single scattering albedo data from nonlinearly mixed VNIR reflectance data and then quantitatively analyzed them using the linear spectral mixture model. Simplifications to the Hapke equation were tested accounting for variables that would be unknown when using satellite data. Mineral mixture spectra from the RELAB spectral library were degraded to test the robustness of the unmixing technique in the face of data that mimic some of the complexities of satellite spectral data collected at Mars. A final test was performed on spectra from shergottite meteorites to assess the technique against real Martian mineral mixtures. The simplified Hapke routine produced robust abundance estimates within 5–10% accuracy when applied to laboratory standard spectra from the synthetic mixtures of igneous minerals in agreement with previous studies. The results of tests involving degraded data to mimic the low spectral contrast of the Martian surface and the lack of a priori knowledge of the constituent mineral spectral endmembers, however, were less encouraging, with errors in abundance estimation greater than 25%. These results cast doubt on the utility of Hapke unmixing for the quantitative analysis of VNIR data of the surface of Mars.

INTRODUCTION

At present, Martian meteorites represent the only samples of Mars available for study in terrestrial laboratories. To date, almost 200 individual meteorites, representing about 100 different specimens, have been identified and confirmed as originating from Mars on the basis of their noble gas and oxygen isotope analyses (International Society of Meteoritics and Planetary Sciences 2017). However, the majority of our understanding of the geochemistry of Mars is through the use of data from orbital spacecraft and a handful of lander missions. To link the detailed geochemical analyses of Martian meteorites to the geological evolution of Mars, it is necessary to have the sample context provided by knowledge of the source location of the meteorites.

All but one of the Martian meteorites are igneous in origin, thus providing a first constraint on their possible source locations on Mars. Two of the most fundamental first order measurements on these samples are the crystallization and ejection ages. Together these ages provide a second constraint on source location on Mars. However, due to the uncertainties caused by bulk versus mineral grain crystallization age, and natural inhomogeneity within a single geological unit (Nyquist et al. 2001), the ejection ages offer the most definitive age for identifying the source location by matching to the age of an impact crater, which has recently been attempted for the shergottites. The clustering of young ejection ages for Martian meteorites suggests that their ejection was caused by possibly as few as five to eight impacts all within the last 20 Ma (Nyquist et al. 2001).

To identify the specific source location of Martian meteorites, it is necessary to introduce a third constraint of geochemistry. Laboratory analyses have provided the mineralogical composition of Martian meteorites in terms of elemental and mineral abundances. At Mars, most of our compositional information is derived from orbital hyperspectral data at visible and near-infrared (VNIR) and thermal-infrared (TIR) wavelengths. These data comprise pixels that are a combination of separate components, due to rocks being made up of different mineral grains. Deriving mineral abundances from these data requires the quantitative decomposition, or "unmixing," of these mixtures. The procedure of spectral unmixing typically involves first decomposing into a collection of constituent spectra, or endmembers, before determining the corresponding abundances of these endmembers (e.g., Keshava and Mustard 2002). However, at the shorter VNIR wavelengths, where we have the highest resolution orbital data at Mars, most common minerals are relatively transparent, leading to volume scattering within and between mineral grains of different species and therefore reflectance spectra that are a nonlinear combination of the minerals at the surface (e.g., Keshava and Mustard 2002). Deconvolving these spectral signatures with nonlinear unmixing models is a complicated, computer-intensive, and potentially nonunique process (e.g., Hapke 1981; Mustard and Pieters 1989; Dobigeon et al. 2014; Pilorget et al. 2016; Lapotre et al. 2017).

Despite the inherent complexities, recent studies have made some headway into nonlinear unmixing in the VNIR (e.g., Broadwater et al. 2009; Bioucas-Dias et al. 2012; Heylen et al. 2014). However, attempts to apply these methods to Mars data are limited (e.g., Goudge et al. 2015) due to the added complexities of a lack of ground-truth data, the pervasive layer of fine particle dust that covers the planet, and less robust atmospheric and photometric corrections. Therefore, attempts are ongoing to geochemically tie these meteorites to their source locations on Mars, meaning that the fundamental geological context is lacking in detail. This lack of context means that the information gleaned from Martian meteorites cannot be used with confidence in studies of the geological, and astrobiological, evolution of Mars. The goal of our work was to help improve geochemical techniques aimed at unmixing VNIR data to return better estimates of igneous mineral abundances, for use in future studies to determine the source location of Martian meteorites to a higher degree of confidence. In this study, we specifically test the validity of the Hapke Radiative Transfer Model as a method of dealing with the nonlinearity of the spectral mixtures of igneous minerals that comprise the bulk of the surface of Mars. Through the unmixing of VNIR data of Martian meteorites and known mixtures from laboratory spectral databases, we offer recommendations for future application of these methods.

BACKGROUND

Mineralogy of Mars

Several recent reviews have summarized the geochemistry (e.g., McSween and McLennan 2014), mineralogy (e.g., Ehlmann and Edwards 2014), and petrology (e.g., McSween 2015) of Mars and Martian meteorites. There have also been updates (e.g., Murchie et al. 2009) to the global paradigm regarding how the geochemistry of the Martian surface has evolved during the history of Mars, with aqueous alteration of particular interest (Bibring et al. 2005, 2006). Given that the main aim of our study was to ultimately help constrain the source location of Martian meteorites, we are concerned here with primary igneous mineralogies, rather than secondary alteration phases. Furthermore, we limit ourselves here to the largest spectral database available for Martian meteorites, that of the shergottites. These samples are essentially basalts and gabbros that have formed from subalkaline magmas (McSween 2015), and so their bulk mineralogy is dominated by olivine, plagioclase (transformed into maskelynite through shock during impact ejection), and pyroxene (pigeonite and augite) phases. Other accessory minerals have been identified in Martian meteorites, but typically at abundances too low to be identified with VNIR spectroscopy. Despite having a bulk mineralogy that is similar to the ancient primary crust of Mars, cosmogenic nuclide ages reveal that these samples formed relatively late in the history of Mars, and may not be representative of the whole Martian crust (McSween et al. 2009). However, improvements in spectral unmixing techniques may allow us to better understand the source location, and geologic context, for Martian meteorites.

Mineral Spectroscopy

The characterization of minerals through their VNIR reflectance spectra is a mature and long-standing field of study (e.g., Hunt and Salisbury 1970; Cloutis 1996; Clark 1999). VNIR spectroscopy is one of the main techniques of mineralogical identification in the exploration of Mars through the use of hyperspectral imaging instruments such as NASA's Compact Imaging Spectrometer for Mars (CRISM) (Murchie et al. 2007) and ESA's Observatoire pour la Minéralogie, l'Eau, les Glaces et l'Activité (OMEGA) (Bibring et al. 2004).

Minerals are primarily characterized through the measurement of the peak wavelength, shape, and depth of their absorption features. For the minerals that form the igneous rocks that comprise much of the surface of Mars, the primary spectral absorption bands are a result of crystal field absorptions (Burns 1993). These absorption features are affected not just by the geochemistry of the mineral but also a number of physical features of the sample being investigated such as particle size, etc. (Clark and Roush 1984). Spectral measurements of planetary surfaces are further complicated due to the mixing of different mineral types within surface rocks, sands, and dust. The radiation incident on the surface potentially interacts with more than one mineral and more than one particle both on the surface and in the atmosphere leading to a reflected signal that is a mixture of the different minerals. The dust on Mars is a particular issue due to its widespread nature and fine particle size closer to the wavelengths used in VNIR spectroscopy. This dust is the cause of much of the surface of Mars being inaccessible to VNIR imaging and adds an additional complication to any attempts to model the surface reflectance via radiative transfer models. To accurately identify and quantify the mineral present on a planetary surface therefore requires a method of unmixing these spectral signatures.

Linear Spectral Unmixing

Spectral mixture analysis (SMA) is a well-established technique for extracting qualitative and quantitative information from hyperspectral data. The bulk of the field has focused on linearly mixed spectra (e.g., Keshava and Mustard 2002; Bioucas-Dias et al. 2012; Quintano et al. 2012; Schmidt et al. 2014; Li et al. 2015), such that would occur when materials are spatially distinct on the ground but combined in a single pixel of a detector. This assumption that the measured spectra is a linear combination of a fixed number of endmembers, enables the quantification of these endmember materials via Equation 1, provided their spectra are known,

$$\boldsymbol{r} = \boldsymbol{aE} \tag{1}$$

where $\boldsymbol{r}$ is the reflectance spectra matrix, $\boldsymbol{E}$ is the matrix of the individual endmember spectra, and $\boldsymbol{a}$ is the matrix containing the abundance of each endmember. The conversion of reflectance data into single scattering albedo via the Hapke equation (see the Hapke Radiative Transfer Model section) allows nonlinearly mixed spectra to be modeled as linear mixtures substituting the $\boldsymbol{r}$ in Equation 1 for $\boldsymbol{w}$, the single scattering albedo of the mixed spectrum, and the individual endmember reflectance spectra in $\boldsymbol{E}$ for the single scattering albedo (SSA) of each endmember, all of which are calculated via inversion of the Hapke equation. The abundance matrix $\boldsymbol{a}$ becomes the mass fraction of each endmember as represented in Equation 2 rather than the bulk volume abundance calculated when using the linear reflectance data. These mass fractions are a function of the volume abundance (M) as well as the density (ρ) and particle size (d) of each endmember. Equation 2 can be used to calculate the volume abundance from the SSA linear unmixing mass fraction abundance results.

$$w = \frac{\sum \frac{M_i}{\rho_i d_i}}{\sum \frac{M_i}{\rho_i d_i}} w_i \tag{2}$$

Different Unmixing Algorithms

Many different algorithms have been developed to perform the abundance estimation step of the linear SMA procedure. The majority incorporate two key constraints to ensure the results are physically real. These are the Sum-to-One constraint that requires the resulting abundances to add up to 100%, and the non-negative abundance constraint that ensures no physically unrealistic negative abundance values are returned (Keshava and Mustard 2002). In this work, six different programs written in the Matlab programming language are used. All were selected due to their applicability to the problem and open availability. Some are based on the same algorithm but use different computation methods available within Matlab to solve the problem. Multiple algorithms were chosen to test if different results would be returned for them and thus gain an understanding of the potential for nonunique solutions to the linear unmixing problem.

1. *hyperFcls*—Matlab program available in the Matlab toolbox hyperspectralv0.07 (https://github.com/isaacgerg/matlabHyperspectralToolbox). This code is based on the linear least squared algorithm of Heinz and Chang (2001). The sum-to-one and non-negative constraints are implemented within the algorithm and the Matlab function pinv is utilized to solve the least squares problem.
2. *hyperFclsMatlab*—Matlab program available in the Matlab toolbox hyperspectralv0.07. The code is based on the linear least squared algorithm of Heinz and Chang (2001) and utilizes Matlab's inbuilt least squared solver lsqlin.

3. *Linear Mixing Model* (*LMM*) (Heylen and Scheunders 2016)—code based on the linear least squares algorithm of Heinz and Chang (2001). The code is based on the inbuilt Matlab FMINCON optimizer function.
4. *Active Set Unmixing* (*ASU*) (Heylen and Scheunders 2014)—This fully constrained least squares algorithm projects potential solutions to the unmixing problem and uses active set methods to ensure the sum-to-one and non-negativity constraints are adhered to.
5. *Multilinear Mixing Model* (*MLM*) (Heylen and Scheunders 2016)—This algorithm, uniquely in the six used in this work, was devised to work with mixtures where the observed radiation spectrum can be modeled as a series of linear interactions between the endmember particles prior to collection by the detector. Unlike the other five, this algorithm specifically requires the conversion of the reflectance spectra into SSA prior to analysis. The code is based on the inbuilt Matlab FMINCON optimizer function.
6. *Sparse Unmixing via Variable Splitting Augmented Lagrangian and Total Variation* (*SUnSAL_TV*) (Iordache et al. 2012)—This algorithm is the only one utilized in this work that allows for violation of the nonnegative constraint although in practice the results rarely include negative abundances. It is also designed to work with a large endmember library, using sparse regression techniques to account for the fact that when unmixing an image not every endmember will be present in every pixel.

Hapke Radiative Transfer Model

Radiative transfer models aim to describe the interaction between radiation and matter. The Hapke model (Hapke 2012) describes single scattering radiation taking into account the physical and optical parameters of the particles involved and the geometry and wavelength of the radiation. This model has been combined with linear mixture models to estimate the abundances of minerals in intimate binary and ternary laboratory mixtures with reliable accuracy (Mustard and Pieters 1987a, 1989; Li and Milliken 2015; Robertson et al. 2016) and is considered an appropriate model for planetary surfaces (Poulet et al. 2002, 2010; Goudge et al. 2015; Liu et al. 2015; Lapotre et al. 2017). The inherent nonlinearity of the mineral mixtures is dealt with through transformation of the reflectance spectra into SSA spectra via the Hapke Equation 3.

$$r = \frac{w}{4(\mu_0 + \mu)}[\{1 + B(g)\}p(g) + H(\mu_0)H(\mu) - 1] \quad (3)$$

where r is the reflectance spectrum, μ_0 is the cosine of the angle of incidence, μ is the cosine of the angle of emission, g is the phase angle, $B(g)$ is the backscattering function accounting for the opposition effect, and w is the SSA. $H(x)$ is the Hapke approximation to the Ambartsumian–Chandrasekhar function given as:

$$H(x) = \left\{1 - wx\left[r_0 + \left(\frac{1 - 2r_0x}{2}\right)\ln\left(\frac{1+x}{x}\right)\right]\right\}^{-1} \quad (4)$$

where $r_0 = (1 - \gamma)/(1 + \gamma)$ and $\gamma = (1 - w)^{1/2}$. The particle phase function in Equation 3 is represented by $p(g)$, and has been dealt with in a number of ways by different authors. Many have chosen to model the scattering behavior of the particles as isotropic and therefore set $p(g) = 1$ (Mustard and Pieters 1987a; Goudge et al. 2015; Cannon et al. 2017). In the case of mineral mixtures, however, the particle scattering is more likely to follow a nonisotropic model. Hapke (2012) discussed two different functions that can be used to model the nonisotropic scattering behavior of particles within the Hapke equation. The first is the double Henyey–Greenstein function (5):

$$p(g) = \frac{1+c}{2}\frac{1-b^2}{(1 - 2b\cos(g) + b^2)^{3/2}} + \frac{1-c}{2}\frac{1-b^2}{(1 + 2b\cos(g) + b^2)^{3/2}} \quad (5)$$

And the second the Legendre polynomial (6):

$$p(g) = 1 + b\cos(g) + c[1.5\cos^2(g) - 0.5] \quad (6)$$

In both cases, b and c are wavelength-dependent constants that must be calculated for each mineral type involved. The Legendre polynomial has been used in a number of studies (Lucey 1998; Liu et al. 2015; Sklute et al. 2015) and has been shown to give accurate results provided the deviation from isotropic scattering is small (Hapke 2012).

Simplifications Due to Satellite Data Unknowns

The Hapke model includes numerous variables, many of which are difficult to estimate accurately from remote spectral data sets. For this reason, a number of assumptions and simplifications are necessary if this technique is to be applied to satellite hyperspectral data such as that from the CRISM instrument.

The Legendre polynomial (Equation 6) is adopted in this work to model the nonisotropic scattering of the mafic minerals involved. Mustard and Pieters (1989) used multiangle data to calculate the two wavelength-dependent parameters b and c in the Legendre polynomial. Multi-incidence angle data are not available for CRISM full resolution targeted (FRT) data (the highest resolution VNIR data available from Mars and most suitable for quantitative analysis) and so some simplification assumptions must be made. Liu et al. (2015) and Lucey (1998) both adopted fixed values of $b = -0.4$ and $c = 0.25$, both of which are close to the experimentally derived values for these constants across the wavelength range for the olivine, pyroxene, and plagioclase minerals used in this paper (Mustard and Pieters 1989). These fixed values shall be adopted for this work.

The abundance matrix calculated in the unmixing equation when using SSA is more accurately the mass fraction abundance linked to the density and particle size of the related mineral endmember. Density values for common minerals are widely available, although these values, particularly for minerals with a wide range of geochemical compositions, can vary. Mean density values shall be taken for each mineral endmember from this existing literature. Attempts have been made to infer particle sizes from OMEGA data using a look-up table approach (LUT) for scenes that are dominated by dust, CO_2 ice, and water ice (Bernard-Michel et al. 2009). These three endmembers show a high degree of spectral difference from each other and little variance in reflectance spectra due to particle size. However, mafic mineral spectral signatures are more highly correlated and the utility of this LUT technique has not been demonstrated with such data. The MP89 laboratory samples used in the Hapke unmixing studies referenced in this paper have all been ground to a maximum particle size of 75 μm, the size of very fine sand, silt, and clay. Grain size analysis by the rovers Spirit and Curiosity show that in Gusev crater (Herkenhoff et al. 2004) and Gale crater (Yingst et al. 2013, 2016), respectively, the grains that comprise the surface range from fine sand to cobbles over the length scales of a CRISM pixel. It is thus a justified assumption to consider mixture particles to be of a large size range, homogenous across the present endmembers and therefore due to the unlikelihood of calculating the actual particle sizes in a specific CRISM image remove this variable from the Hapke unmixing routine.

To summarize, the Hapke equation shall be used to convert reflectance data to SSA data with the simplification of $H(x)$ given in Equation 4, with $B(g) = 0$ (making the assumption that the backscatter effect is negligible, an acceptable assumption provided the phase angle is greater than 15° (Mustard and Pieters 1987b, 1989), and with $p(g)$ as given by Equation 6, with fixed constants $b = -0.4$ and $c = 0.25$. These converted SSA mixture data sets shall then be unmixed using the six linear unmixing algorithms detailed in the Different Unmixing Algorithms section and a spectral endmember library. In each unmixing operation, every member of the endmember library will be available to the unmixing algorithm and thus an abundance for every endmember in the library will be calculated. The resulting mass fraction abundance values shall be converted to volume abundance using Equation 2. In dealing with the abundance results from the unmixing algorithms, it shall be assumed that particle sizes cover a uniform range across all endmembers and can therefore be removed from the mass fraction transformation. Endmember densities shall be included in this volume abundance calculation and shall be taken from published average values for the mineral species each endmember is identified as (e.g., olivine, plagioclase, clinopyroxene, etc.).

METHODS

The aim of this paper was to test the accuracy and utility of the Hapke model of SMA for the purposes of analyzing hyperspectral imagery from Mars. A number of spectral mixture and spectral endmember data sets were constructed from VNIR reflectance data collected at the RELAB facility (see the RELAB Public Spectral Library section). These were converted from reflectance to SSA via the Hapke equation (Equation 3). The abundance of individual endmembers within spectral mixtures was calculated using these SSA data and the linear unmixing equation (Equation 1) expressed using six different computer programs. Five experiments were constructed to investigate different complications that affect the analysis of spectral data collected remotely (see Fig. S1 in supporting information for full workflow). These five experiments are:

1. Simulated instrument noise
2. Decreased spectral resolution
3. Decreased spectral contrast
4. Unknown spectral endmembers
   a. Use of an endmember library larger than the actual number of endmembers present
   b. Use of an endmember extraction algorithm
5. Spectrally neutral and minor additional endmembers (shergottite meteorites)

Data sets

RELAB Public Spectral Library

The Reflectance Experiment Laboratory (RELAB) at Brown University is a NASA-supported research facility to

enable users to collect reflectance spectra from geological materials (Pieters and Hiroi 2004). A bidirectional reflectance spectrometer enables measurements to be taken between 0.3 and 2.6 μm at varying incidence and emission angles. A massive public database is available comprised of spectra collected by the numerous researchers that have utilized the facility over the past three decades. This database contains over 20,000 spectra as of December 2014. Spectra were selected from this library to create three data sets for use in this work, two mixture data sets and one primary endmember library from which sublibraries were selected as appropriate for the relevant experiment. For each data set created, the spectra selected were collected with a 30° incidence angle and a 0° emission angle. All samples had been powdered prior to analysis and the detector was set to collect wavelengths encompassing the range of at least 0.4–2.5 μm. However, not all spectra selected had been collected at the same wavelength resolution. To enable use in the Hapke unmixing pipeline outlined in the Simplifications Due to Satellite Data Unknowns section, selected spectra for all three data sets were initially resampled to the same wavelength resolution, that of the hyperspectral CRISM (Murchie et al. 2007) instrument operating in FRT mode, and where necessary trimmed to cover only the wavelength range 0.4–2.5 μm.

Mustard and Pieters Binary and Ternary Mafic Mixture Spectra

One of the earliest and most prominent attempts to use Hapke radiative transfer modeling in the quantitative analysis of mafic mineral mixtures is the work of Mustard and Pieters (1987a, 1987b, 1989). In these papers, binary and ternary mixtures of olivine (Fo92), enstatite (En88Wo00Fs11), and anorthite (An78) were created and spectra were collected in the RELAB facility from each mixture and the three mineral endmembers. The version of the RELAB database interrogated for this work included 23 mixture spectra and the three endmember spectra from these works, enabling investigation of the effect of variables other than unknown endmembers in the abundance estimation problem. This data set shall be referred to as the MP89 data set for the rest of this paper (Fig. 1).

Shergottite Spectra

The shergottites are the most abundant class of Martian meteorites in the world's collection. The majority have not been analyzed with VNIR reflectance spectroscopy. Spectra from powdered whole rock samples of eight shergottites are available in the RELAB spectral library (ALHA77004, EETA 79001,

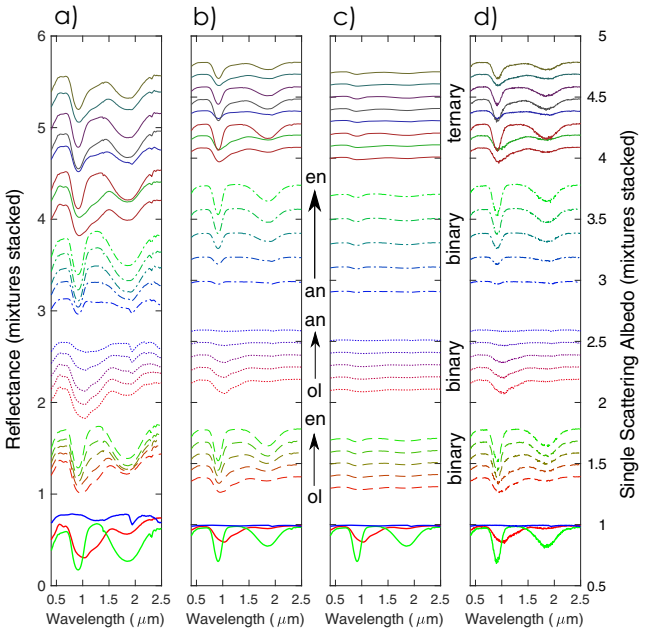

Fig. 1. MP89 data set mixture and single mineral spectra: (a) original reflectance values, (b) transformed single scattering albedo spectra, (c) transformed single scattering albedo spectra created from the mixture spectra scaled to mimic typical CRISM reflectance values, (d) transformed single scattering albedo spectra from reflectance data with additional 35 dB of Poisson white noise. Single mineral spectra are plotted at the bottom of the figures and are not stacked. Mixtures are plotted above and are stacked. Spectra are grouped by mixture type with color grading indicating the proportion of endmember minerals present. Dashed lines = olivine + enstatite, dotted lines = olivine + anorthite, dash-dot lines = anorthite + enstatite, solid lines = olivine + enstatite + anorthite. Spectra in order from bottom to top are: PO-CMP-017/C1PO17/Olivine (red—Fo92), PE-CMP-012/C3PE 12/Enstatite (green—EN88Wo00Fs11)), PA-CMP-012/C1PA12/ Anorthite (blue—An78), XO-CMP-015/C1XO15/Olv90 + Enst10, XO-CMP-016/C1XO16/Olv75 + Enst25, XO-CMP-017/C1XO17/ Olv50 + Enst50, XO-CMP-013/C1XO18/Olv25 + Enst75, XO-CMP-019/C1XO19/Olv10 + Enst90, XO-CMP-020/C1XO20/ Olv90 + Anor10, XO-CMP-021/C1XO21/Olv75 + Anor25, XO-CMP-022/C1XO22/Olv50 + Anor50, XO-CMP-023/C1XO23/ Olv25 + Anor75, XO-CMP-024/C1XO24/Olv10 + Anor90, XA-CMP-001/C1XA01/Anor90 + Enst10, XA-CMP-002/C1XA02/Anor75 + Enst25, XA-CMP-003/C1XA03/Anor50 + Enst 50, XA-CMP-004/C1XA04/Anor25 + Enst75, XA-CMP-005/ C1XA05/Anor10 + Enst90, XO-CMP-030/CMX O30/Olv67.6 + Anor16.2 + Enst16.2, XO-CMP-031/C1XO31/Olv16 + Anor 16.1 + Enst67.9, XO-CMP-032/C1XO32/Olv1 6.2 + Anor67.8 + Enst16, XO-CMP-033/C1XO33/Olv42.1 + Anor16.1 + Enst41.8, XO-CMP-034/C1XO34/Olv16.4 + Anor41.8 + Enst41.8, XO-CMP-035/C1XO35/Olv42 + Anor41.9 + Enst16.1, XO-CMP-036/ C1XO36/Olv33.3 + Ano r33.6 + Enst33, XO-CMP-030/CMX O30/Oliv67.6 + Anor16.16 + Enst16.24, (RELAB Sample ID/RE LAB Spectrum ID/Mineral Name and Abundance percentage where Olv = olivine, Enst = enstatite, and Anor = anorthite). (Color figure can be viewed at wileyonlinelibrary.com.)

LEW 88516, Los Angeles, QUE 94201, Shergotty, Y-984028, and Zagami) (Fig. 2). Additional spectra from individual minerals found within some of these meteorites are also available within the RELAB database. These were added to the mafic spectral library (see the Mafic Spectral Library section) for unmixing of the shergottite spectra.

Bulk mineralogy of the shergottites examined at RELAB is available and has been used to validate the abundance estimations from the shergottite spectra within this work (Table 1).

The shergottite spectra were selected to test the accuracy of the unmixing routine in the face of spectrally neutral glass and impact melt, and the minor presence of accessory minerals. The presence of these endmembers is presumed to be common on the Martian surface and thus if this technique is to be used to analyze CRISM data, it must be able to cope with this additional mixture complexity.

Mafic Spectral Library

A large mafic mineral endmember library was constructed by selecting spectra from pyroxene, olivine, plagioclase, glass, and impact melt samples. Shocked and heated samples were included as were natural and synthetic. For olivine and pyroxene, the synthetic samples included were specifically chosen to ensure the full range of the respective solid solution series. Collections of spectra produced by the same researcher were prioritized to minimize user-induced variation in the spectra. The three spectra of the samples used to create the MP89 mixtures were included in this mafic spectral library. The full list of the spectra used is included in the supporting information accompanying this article.

Description of Experiments

A baseline test was run using the MP89 data set resampled to CRISM FRT wavelengths (high spectral resolution) and the three endmember spectra (also resampled to CRISM FRT wavelengths) taken from the three mineral samples used to create the synthetic mixtures. This provided a check of the simplified Hapke routine used together with the six linear unmixing algorithms against results from previous works. It also provided a gauge of the limits of accuracy expected from the experiments using degraded or imperfect data that followed.

Simulated Instrument Noise

Laboratory-collected VNIR reflectance spectroscopy data have a high (generally >500) signal-to-noise ratio (SNR). Similar data collected via satellite instruments tend to have a lower SNR due to a number of factors including atmospheric interference, instrument artifacts, and instrument noise (Berman et al. 2017). Preprocessing of the data can remove much of the first two of these unwanted signals but underlying instrument noise will remain. The CRISM instrument was designed to have an SNR of at least 400 at 2.3 μm and at least 100 at other

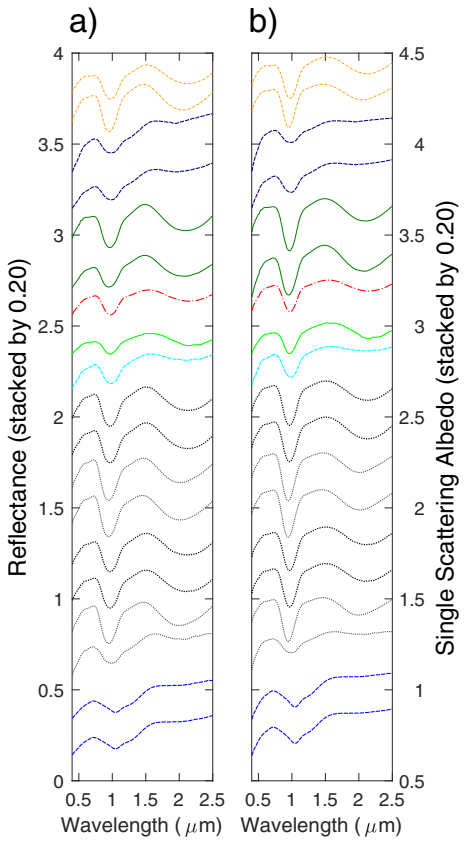

Fig. 2. RELAB whole rock powdered shergottite data set spectra, plot on left (a) in original reflectance values, plot on right (b) the transformed single scattering albedo spectra. Line weights and colors denote meteorite subtype: blues = intermediate ultramafic poikilitic, grays/blacks = intermediate permafic olivine-phyric and mafic, greens = enriched mafic diabasic, reds = depleted mafic diabasic, and yellows = enriched mafic intersertal. Spectra in order from bottom to top are: ALHA77005/DD-MDD-026/BKR2DD026, ALHA 77005/DD-MDD-026/C1DD26, EETA 79001A/DD-MDD-019/C1DD19, EETA 79001A/LM-LAM-007-PA/CALM07, EETA 79001B/LM-LAM-007-PB/C2LM07, EETA 79001B/LM-LAM-007-PB/CBLM07, EETA 79001A/MT-JLB-004-A/BKR1MT004A, EETA 79001A/MT-JLB-004-A/C1MT04A, EETA 79001B/MT-JLB-004-B/BKR1MT004B, EETA 79001B/MT-JLB-004-B/C1MT04B, LEW 88516/DD-MDD-022/C1DD22, Los Angeles/DD-MDD-027/C1DD27, QUE 94201/DD-MDD-024/C1DD24, Shergotty/DD-MDD-061/C1DD61, Shergotty/LM-LAM-021/C1LM21, Y-984028/DD-MDD-117/C1DD117, Y-984028/DD-MDD-118/C1DD118, Zagami/DD-MDD-025/C1DD25, Zagami/MB-LAM-049-P/CPMB49 (Meteorite ID/RELAB Sample ID/RELAB Spectrum ID). (Color figure can be viewed at wileyonlinelibrary.com.)

Table 1. Shergottite bulk mineral abundances. Each line represents the results from a different study or analysis.

Meteorite	Ref	PX	CPX	OPX	Aug	Pig	Oli	Plag	Mask	Meso	Other
ALHA77004	a	35	11	26			55		8	1	2
	b						52		10		1
EETA79001A	c			3.4	3.2	62.8	10.3		18.3		2.2
EETA79001A	c			5.7	6.5	60.7	7.2		15.9		4
EETA79001A	c			7.2	8.5	54.5	9.1		17	0.7	3.8
EETA79001B	c				11.6	54.4			28.2	1.8	1.8
EETA79001B	c				23.9	32.2			29.4	0.7	4.2
EETA79001B	c				24.5	31.8			29.6	0.7	3.8
LEW 88516	d	37					45.9		7	9.9	3.1
	e	22					57		16	5	6
Los Angeles	f	43.7					1.9		44.8	7.3	8.1
	f	37.7					4.2		43.6	10.9	11.2
	g	41.6					1.9		45	11.5	9
	h	40.9							43.9	5.2	3
QUE 94201	i				10.1	33.7			46	9.9	9.8
	j		42						43	11	16
	k	52.3					1.7		41.3	4.6	7
Shergotty	l	70.5							23.9	3.6	0.8
	l	69.1							22.7	5.5	0.3
	m	68.9							24	3.1	4.4
	n	70							20	4.2	2.2
	o		67.5						24	7.9	6.2
	p	66.5						29.8		2.7	4.1
Y-984028	q	72					25		1	3	2
	q	17					61		10	8	10
	q	2					27			71	4
Zagami	l	69.7			37.5	37.5	0.8		24.7	3.4	0.8
	l	76.3							18.8	2.8	1.1
	r	77.7							17.6	4.5	3.1
	r	74.3							18.8	6.7	3.4
	r	76							18.6	5.3	3.4
	r	80.4							10.3	9.1	5.8
	s								18	5.2	3.2

References: a. Antarctic Meteorite Working Group (1981), b. Ma et al. (1981), c. McSween and Jarosewich (1983), d. Treiman et al. (1994), e. Gleason et al. (1997), f. Rubin et al. (2000), g. Mikouchi (2001), h. Xirouchakis et al. (2002), i. Mcsween et al. (1996), j. Mikouchi et al. (1998), k. Harvey et al. (1996), l. Stolper and McSween (1979), m. Duke (1968), n. Smith and Hervig (1979), o. Stöffler et al. (1986), p. Lodders (1998), q. Riches et al. (2011), r. McCoy et al. (1992), s. Treiman and Sutton (1992).

Ref = reference study, PX = pyroxene, OPX = orthopyroxene, CPX = clinopyroxene, Aug = augite, Pig = pigeonite, Plag = plagioclase, Mask = maskelynite, Meso = mesostasis, Other = all other minerals present.

wavelengths between 0.4 and 2.6 μm (Murchie et al. 2007). The instrument has been in operation for almost a decade and the SNR is expected to have degraded to approximately 200 at 2.3 μm but have remained around 100 at 0.4 μm (Bultel et al. 2015). Therefore, to better represent instrument data, Poisson-distributed random white noise (Kreisch et al. 2017) was added to the MP89 data set mixture spectra to simulate the equivalent of 35 dB (approximately SNR = 60) (Fig. 1) and 45 dB (approximate SNR = 170) worth of SNR to test how the Hapke unmixing copes with noisy data.

Decreased Spectral Resolution

CRISM has a number of operating modes. The primary mode for in-depth mineralogical investigations is the FRT that produces images with ~18 m pixels and spectral resolution of ~7 nm (Murchie et al. 2007), broadly similar to that of the laboratory data used in previous Hapke unmixing studies (e.g., Mustard and Pieters 1989). This high precision product has been produced for approximately 2% of the Martian surface. A second product is the multispectral mapping mode (MSP). This mode produces data with a reduced spectral resolution of only 74 bands spaced approximately 30 nm apart. The MSP images are also of a reduced pixel size of ~200 m (Murchie et al. 2007) but do cover the majority of the surface. The paucity of coverage in the FRT data limits its use for global mineralogical surveys, whereas this is not such an issue for the MSP data set. The spectral signatures of the

bulk mafic minerals that make up the surface of Mars, and are considered in this work, are dominated by broad absorption features that are still generally evident in 30 nm resolution spectra. It is therefore worth investigating if the Hapke unmixing is accurate in the face of reduced spectral resolution. The MP89 data set (both mixtures and endmembers) outlined in the Data Sets section shall be resampled from CRISM FRT wavelengths to CRISM MSP wavelengths prior to the Hapke unmixing analysis and the results presented.

Decreased Spectral Contrast to Mimic Average Spectrum From Martian Surface

A key difference between laboratory spectral data and satellite spectral data is the spectral contrast and average reflectance. Satellite data tend to have a lower average reflectance and lower spectral contrast than comparable laboratory data. The average reflectance of the Martian surface in OMEGA data (Schmidt et al. 2014) and Infrared Spectrometer for Mars (ISM) data (Vincendon et al. 2007) is 0.35 in the wavelength range 1.0–2.5 μm. To ensure the MP89 igneous mixture spectra better represented the average reflectance that would be returned from a Mars orbiting spectrometer, a flat spectrum of 0.35 reflectance was added to each mixture spectrum in the data set at a ratio of 90/10 prior to the Hapke SSA conversion as per the work of Schmidt et al. (2014). This resulted in spectrally flatter mixture spectra that better mimicked the data returned from Mars compared to the original laboratory data (Fig. 1c). The flat endmember is not supposed to perfectly represent an endmember present in a Martian scene, although it is very similar to reflectance spectra acquired from dust-dominated pixels (Poulet et al. 2008). The flattened MP89 spectra were unmixed using an endmember library comprising the three actual endmembers and the additional synthetic flat endmember.

Unknown Spectral Endmembers

Much of the validation work that has been published showing the accuracy of the Hapke model in quantitatively analyzing mineral mixtures has started with the assumption that the endmember minerals are spectrally and physically well-characterized and known a priori (Mustard and Pieters 1987a, 1989; Robertson et al. 2016). When analyzing synthetic mixtures in the laboratory, the spectral signature of the specific sample minerals used can be collected prior to the creation of the mixtures and thus used in any unmixing procedure (as is the case with the MP89 data set and its three endmembers). When analyzing satellite data, however, these precise spectral endmembers are unknown and difficult to estimate, but to perform abundance estimation they are required. The presence of common mafic minerals can be inferred from satellite spectral imagery using techniques such as spectral parameter mapping (Pelkey et al. 2007; Viviano-Beck et al. 2014). The spectral signatures of mafic mineral types, e.g., pyroxene, olivine, plagioclase, all share common features allowing them to be positively identified as that particular mineral type. However, due to geochemical, physical, and environmental variations, there is a wide range of diversity that can be seen within the spectral signatures from each mineral type group, with every natural sample returning a slightly different signature unless preprepared to remove some of these variants. This, together with the range of particle sizes, orientations, and distributions that can be present in a planetary regolith can complicate the identification of specific individual endmember minerals from remote measurements. There are various methods that have been used to work around this issue, the two main ones are, (1) using a large endmember library of laboratory spectra that hopefully contains the endmembers present as well as many others that are not, and (2) extracting spectral endmembers from within the mixture data set itself.

Use of Massive Laboratory Spectral Library

Geological knowledge and techniques such as spectral parameter mapping can enable a good estimate to be made as to the mineral types present in a remote scene. Spectral representations of these minerals can then be taken from a spectral library such as the RELAB spectral database to build the unmixing endmember data set. Using a large endmember library of laboratory spectra is one solution to the problem of unknown spectral endmembers that has been utilized by a number of authors when using Hapke modeling to quantitatively analyze hyperspectral data (e.g., Li and Milliken 2015). Using a large endmember data set could encompass the geochemical and spectral variation that may be present in the mixtures but the larger the number of endmembers involved, the heavier the computational burden and the higher the chance of the algorithms returning incorrect results due to the nonunique nature of the fitting techniques used. The mafic endmember library described in the Mustard and Pieters Binary and Ternary Mafic Mixture Spectra section was used as an initial large endmember library and simple methods for trimming this down investigated.

Use of Endmember Extraction Algorithms

Algorithms designed to extract endmember spectra from mixed hyperspectral image pixels have been the subject of intense research for many years and a vast literature now exists describing them (see reviews for further details, e.g., Bioucas-Dias et al. 2012; Heylen et al. 2014). Many are optimized for specific targets

such as tree canopies or urban scenes and are thus inappropriate for analyzing intimate mineral mixtures. One algorithm that is openly available and suitable for nonlinearly mixed mineral data is the simplex identification via split augmented Lagrangian (SISAL) algorithm (Bioucas-Dias 2009). This algorithm is optimized for use on linearly mixed data but has shown reasonable results with nonlinearly mixed data (Harris et al. 2016) and specifically when used in conjunction with Hapke SSA transformed data sets (Nascimento and Bioucas-Dias 2010). A simplex is fit around the spectral reflectance data in N-dimensional space where N is the number of spectral bands present. The volume of this simplex is minimized and each vertice taken as a "pure" (i.e., a single/unique endmember) spectral endmember of the mixtures in the data set. This is a common approach in endmember estimation algorithms (Bioucas-Dias et al. 2012) but in SISAL, the vertices do not have to correspond to any one of the input spectra, i.e., it is not assumed that for each endmember there is at least one "pure" pixel composed entirely of a single material. In the case of Mars and CRISM data, this "pure" pixel assumption would be unrealistic and SISAL accounts for this. In using SISAL to extract spectral endmembers for use in unmixing a number of issues must be noted. The spectral endmembers that are extracted do not necessarily share a one-to-one correspondence with the physical reality of the input data set and the spectral signatures of the actual physical endmembers. It is possible to extract endmember spectra that do not match any real mineral reflectance spectra. Second, the number of endmembers to extract must be known in advance and fed into the algorithm. This is not a trivial task. Finally, the algorithm struggles to extract endmembers with low spectral contrast and low reflectance. These limitations shall be taken into consideration when evaluating this algorithm as a method of estimating the endmembers for use in the unmixing routine.

Additional Minor and Spectrally Neutral Endmembers

The Martian surface consists of more than just olivine, pyroxene, and plagioclase, although from analysis of the only samples we have of the surface, the Martian meteorites, these are the dominant minerals. Minor accessory minerals and altered versions of the bulk mafic minerals are also present and thus how well the Hapke unmixing routine performs in the face of these more complex mixtures should be established. Spectra from the shergottite meteorites (Fig. 2) are used to perform this experiment using a large endmember library containing examples of olivine, pyroxene, and plagioclase, as well as glasses and impact melts. Additional minerals are not included in the library despite contributing up to 10% volume of the meteorites. No single accessory mineral (e.g., chromite, phosphate, sulfide, carbonates) makes up more than 5% (Table 1 and references therein) and it is therefore expected that they will not be contributing to the spectral signature in a significant manner.

Accuracy Metrics

Actual Abundance Versus Estimated Abundance

In the experiments using the MP89 data set, the mineral endmember abundances in each mixture are known. The accuracy of the unmixing can therefore be judged by comparing these volume abundances directly. Bulk mineralogy details for the shergottite data set shall be used to provide validation for these unmixing results.

Spectral Reconstruction RMSE and SAM

When dealing with nonlaboratory data, the actual volume abundances of the constituent endmembers in a scene is unknown. A method is needed therefore to judge the accuracy of the unmixing routine when it is applied to satellite data. The common method is to reconstruct the input spectra using the endmember spectra and the unmixing results and compare these reconstructions to the original collected spectra. Common metrics to measure how similar these two sets of spectra are include the root mean squared error (RMSE) and the spectral angle mapper (SAM) (Kruse et al. 1993). Both of these metrics will be applied to all results in this paper and the applicability of this accuracy metric discussed.

RESULTS

Baseline Results

The MP89 data set and its three associated endmember spectra were all converted from reflectance data to SSA data using the Hapke routine outline in the Background section. These were then fed into the six unmixing programs described in the Simplifications Due to Satellite Data Unknowns section and the resulting volume abundances calculated using Equation 2 compared to the actual abundance values. RMSE and SAM values were calculated from the reconstruction of the SSA mixture spectra using the input endmembers and the estimated abundances. The majority of the results for all unmixing programs were within 5% error and, with the exception of one mixture unmixed with MLM, all were within 10%. The results from hyperFcls, ASU, LMM, and hyperFclsMatlab were all identical with 14 out of 23

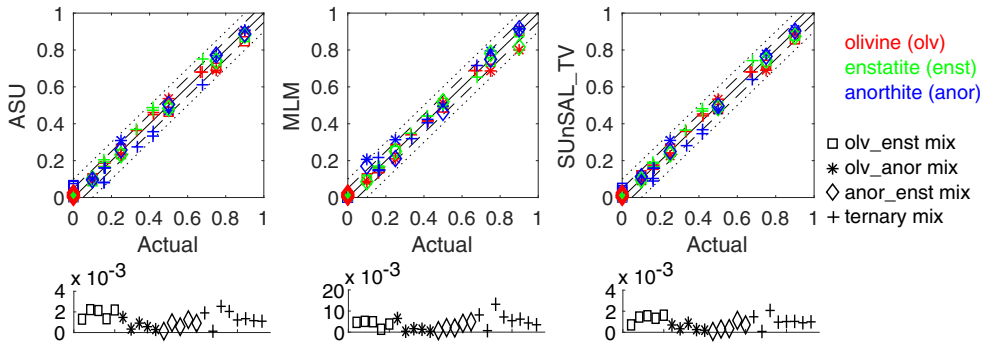

Fig. 3. Volume abundance estimates from three unmixing programs applied to the Hapke transformed SSA CRISM FRT MP89 mixture spectra together with the three actual endmember spectra, compared to the actual mineral endmember abundance values for each mixture in the MP89 data set. Red = olivine (olv), green = enstatite (enst), blue = anorthite (anor), and squares = olv + enst mixture, asterisks = olv + anor mixture, diamonds = anor + enst mixture, plus signs = ternary mix of olv + enst + anor. Solid, dashed, and dotted lines represent a one-to-one fit, a 5% error, and a 10% error in volume abundance estimation, respectively. Under each abundance plot are the associated RMSE results comparing the input SSA spectra to those reconstructed from the input endmembers and the estimated abundance results from the relevant unmixing program. The *x*-axis represents the 23 spectra in the MP89 data set in the order listed in the caption for Fig. 1 with the symbols again representing the mixture type as in the associated volume abundance plots. The results for the unmixing programs LMM, hyperFcls, and hyperFclsMatlab were all identical to those for ASU and are not shown here. The programs work with all three input endmembers for each spectrum in the input data set and are therefore free to assign a nonzero abundance for all three endmembers to all mixtures, even those that are binary mixtures. This results in points on the abundance plots where a nonzero abundance has been estimated for a mineral that is not actually present in a particular binary mixture. This point applies to all abundance plots in this paper. (Color figure can be viewed at wileyonlinelibrary.com.)

mixtures returning within 5% error across the three endmembers and the remaining nine mixtures all within 8% error. SUnSAL_TV returned results within 5% error for 19 out of 23 mixtures and with a maximum error of 8% in the remaining four mixtures. The abundance estimates from MLM were within 5% error for 20 of the 23 mixtures with one mixture having an abundance error of 11%. These results are in broad agreement with those of previous works (Mustard and Pieters 1987a, 1989; Li and Milliken 2015). No trend is evident in the abundance errors in the binary mixtures; however, with the ternary mixtures, all algorithms with the exception of MLM underestimate the abundance of anorthite present in each mixture and overestimate the olivine and enstatite (Fig. 3).

RMSE and SAM values comparing the original MP89 SSA spectra to those reconstructed with the input endmembers and the resulting abundance estimates were highly correlated with a regression fit $R^2 > 0.98$. This correlation was found for all RMSE and SAM values for all experiments and thus for the remainder of this paper only the RMSE values shall be discussed. RMSE values in this case were low (Fig. 3) ranging from 1.28×10^{-4} to 2.54×10^{-3} for the ASU and matching algorithms, 4.06×10^{-4}–1.32×10^{-2} from the MLM results, and 7.64×10^{-5}–2.07×10^{-3} from the SUnSAL_TV results. However, the values did not follow a pattern of agreement with the abundance errors; for example, the spectra with the lowest unmixing abundance error were not necessarily the spectra with the lowest RMSE value.

Simulated Instrument Noise and Decreased Spectral Resolution

Poisson white noise was added to the MP89 CRISM FRT resolution reflectance data set to mimic a CRISM image SNR of 35 and 45 dB. These "noisy" data sets were then converted to SSA and unmixed using the six unmixing programs and the three actual "clean" endmembers. A second test was constructed using the MP89 data set with down-sampled spectral resolution matching that of the CRISM MSP data products. The estimated abundances from unmixing all three resulting mixture data sets (35 dB white noise, 45 dB white noise and MSP resolution) showed the same abundance error patterns as for the baseline case with error increases of at most 1–2%. Further details and figures are available in the supporting information.

Decreased Spectral Contrast to Mimic Average Spectrum From Martian Surface

Spectral contrast and overall reflectance were lowered through the addition of a flat neutral spectrum as detailed in the Decreased Spectral Contrast to Mimic Average Spectrum from Martian Surface section

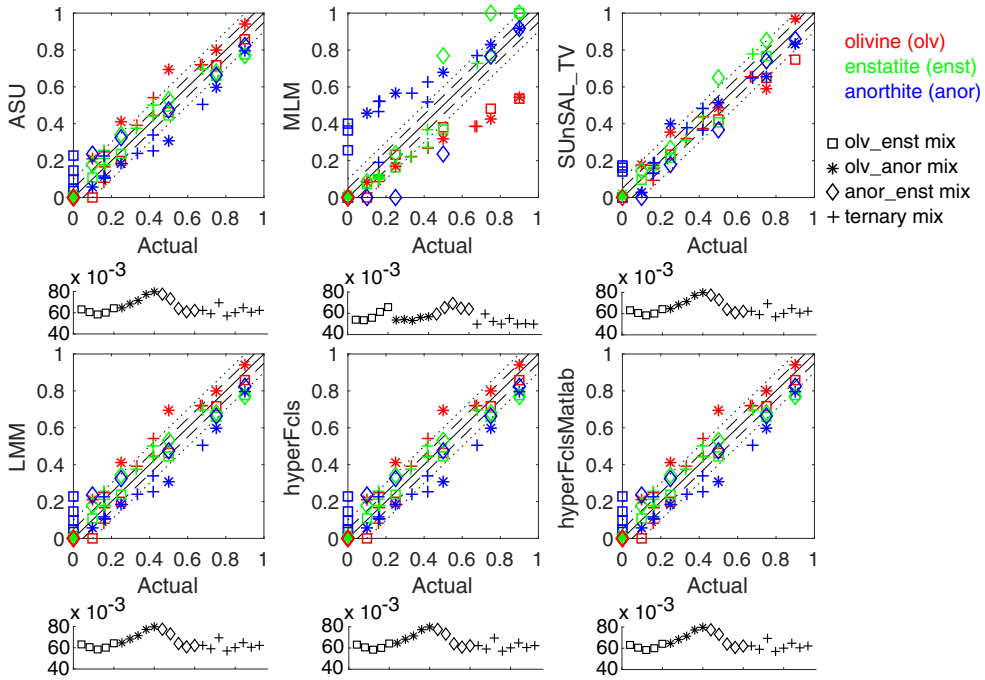

Fig. 4. Volume abundance estimates from six unmixing programs applied to the Hapke transformed SSA CRISM FRT MP89 spectra flattened to mimic reduced spectral contrast of CRISM images together with the three actual endmember spectra plus the flat scaling endmember, compared to the actual mineral volume abundance values for each mixture in the MP89 data set. The volume abundance estimates have been normalized to remove the estimated fraction of the flat scaling endmember. Red = olivine (olv), green = enstatite (enst), blue = anorthite (anor), and squares = olv + enst mixture, asterisks = olv + anor mixture, diamonds = anor + enst mixture, plus signs = ternary mix of olv + enst + anor. Solid, dashed, and dotted lines represent a one-to-one fit, a 5% error, and a 10% error in volume abundance estimation, respectively. Under each abundance plot are the associated RMSE results comparing the input SSA spectra to those reconstructed from the input endmembers (the three MP89 endmembers and an additional flat endmember) and the estimated abundance results from the relevant unmixing program. The *x*-axis represents the 23 spectra in the MP89 data set in the order listed in the caption for Fig. 1 with the symbols again representing the mixture type as in the associated volume abundance plots. (Color figure can be viewed at wileyonlinelibrary.com.)

(Fig. 1c). The resulting reflectance spectra were converted to SSA using the three actual spectral endmembers from the MP89 data set and the additional flat neutral spectrum, all four of which were also converted to SSA prior to unmixing. All six unmixing programs were applied and RMSE and SAM values were calculated for reconstructed mixture spectra from the results. RMSE values from the ASU, hyperFcls, hyperFclsMatlab, and LMM ranged from 5.70×10^{-2} to 7.97×10^{-2}, from the MLM they ranged from 4.98×10^{-2} to 6.93×10^{-2}, and from the SUnSAL_TV results ranged from 5.70×10^{-2} to 7.97×10^{-2} (Fig. 4).

The abundance results were rescaled using the estimated flat endmember abundance to normalize the three mineral abundance values for comparison to the original mixture abundance fractions (Fig. 4). The results from ASU, hyperFcls, hyperFclsMatlab, and LMM were all identical. Within these results, 5 of 23 mixture abundance estimates were within 5%, a further nine being within 10%, and the remaining nine having a maximum error of 23%. Where there is 33% or more of enstatite in the mixture, the unmixing programs are consistently underestimating its presence in both the binary and ternary mixtures. The MLM algorithm estimates are within 5% error in only 4 of 23 mixtures with an additional six within 10%, and errors as high as 36% in the remaining 13 mixtures. Anorthite is overestimated in 20 of 23 mixtures by MLM, the only cases where it is not overestimated being from the binary anorthite + enstatite mixtures. Where enstatite makes up 50% or less of a mixture it is underestimated, and overestimated when it makes up more than 50%. Olivine is underestimated in every single mixture in which it is present. SUnSAL_TV estimates the mineral abundances within 5% in nine mixtures, within 10% in a further eight mixtures, and with a maximum error of 17% in the remaining six mixtures. Where enstatite is present in more than 50% abundance, it is slightly overestimated and where anorthite is present in more than 50%, it is slightly underestimated. Where no single mineral makes up more than 50% abundance, there is

no consistent pattern to the errors in abundance estimation using SUnSAL_TV. In the ternary mixtures for all algorithms, anorthite is underestimated and enstatite and olivine both overestimated as was also seen in the baseline case. For every one of the algorithms in the binary olivine + enstatite mixtures, every time anorthite is overestimated (i.e., selected to be present in the mixture) and olivine and enstatite underestimated.

Unknown Spectral Endmembers

Use of Massive Laboratory Library

The resampled CRISM FRT resolution MP89 data set were converted to SSA and unmixed using the six unmixing algorithms and the mafic endmember library minus the clinopyroxene, glass, and impact melt endmembers and any endmembers altered by heating or radiation. This left the library with only unaltered orthopyroxene, olivine, and plagioclase endmembers, the three mineral types that are present in the MP89 data set but not just the three specific chemical compositions. Estimated mass fractions for each mineral type were amalgamated and transformed into volume abundances using average mineral density values. The unmixing was carried out with the inclusion of the three actual MP89 spectral endmembers (total endmembers = 275) and without (total endmembers = 272). The hyperFclsMatlab program returned an error assigning an abundance of one to the first endmember and zero to all subsequent endmembers. It was therefore not considered for the rest of this experiment.

With the number of endmembers increased, none of the remaining five unmixing programs returned the exact same results. This is evidence of the nonuniqueness of the potential solutions. To bring down the temporal cost of the programs and to minimize the range of potential solutions, a method of trimming the endmember spectra library was required.

To bring down the number of input endmember spectra (and therefore the computation cost), the library was trimmed to only include those endmembers that had been selected by at least one program, at least once, accounting for at least 1% of one mixture. This process was repeated until no more than 30 endmembers remained. If this trimming criterion ceased to remove endmembers and there were still more than 30 remaining, a second trimming method was used excluding all those spectra that were not selected by all programs accounting for at least 1% of at least one mixture and once again a final of less than 30 endmembers was accepted. Trimming the 272 endmember library (without the actual mixture endmembers present) resulted in a final set of 14 spectra after three trimming procedures. Of these, seven were orthopyroxene, four of which were from enstatite samples. Three olivine spectra were selected of which only one is listed with its chemical composition, Fo100 (close to the Fo92 composition of the actual olivine endmember in the mixtures), and the remaining five were plagioclase, of which one listed its specific plagioclase type as bytownite, an anorthite-rich plagioclase. All five programs gave different results, but all show a similar pattern with overestimation of olivine, especially when it was present in only small amounts or not at all, and an underestimation of anorthite/plagioclase (Fig. 5). The enstatite/orthopyroxene is overestimated in most cases by as much as 20% in the MLM and 12% in the ASU and LMM results. The maximum error across the three endmember minerals ranges from 63% in the MLM estimates to 42% in the SUnSAL_TV estimates. In the majority of the cases where the abundance error is greater than 20%, the olivine and anorthite/plagioclase have been overestimated and underestimated, respectively, by similar amounts. The RMSE values were all of a similar value ranging from as low as 3.54×10^{-4} for SUnSAL_TV results to a maximum 6.08×10^{-2} for the MLM results (Fig. 5). With the exception of the MLM algorithm, the RMSE results spanned roughly only a factor of 10 in their values.

When the actual endmembers are present in the initial library, it also took three iterations to trim to the final endmember set of 27 spectra, three of which are the actual spectra of the minerals used to create this mixture data set. The largest abundance estimate errors come from the SUnSAL_TV results with a maximum error of 46% (Fig. 6). Of the other four programs, the maximum error is 25% from hyperFcls and 21% from ASU, LMM, and MLM. All five programs tend to overestimate the abundance of enstatite/orthopyroxene but by much less than the results from the 272 endmember library, and the anorthite/plagioclase and olivine are underestimated more often than not. For the olivine, this is a reversal of the trend seen in the results from the 272 endmember library. The majority of the results are within 10% error bounds and the three actual endmembers are the most abundantly selected by all programs. The RMSE values are similar for ASU, LMM, hyperFcls, and SUnSAL_TV ranging from 2.82×10^{-5} to 1.65×10^{-3} and range 1.73×10^{-4}–2.65×10^{-2} for MLM (Fig. 6).

Use of Endmember Extraction Algorithms

The endmembers extracted from the simulated CRISM FRT spectral resolution MP89 mixture data set using the SISAL algorithm when assuming three endmembers were used to unmix the MP89 data set.

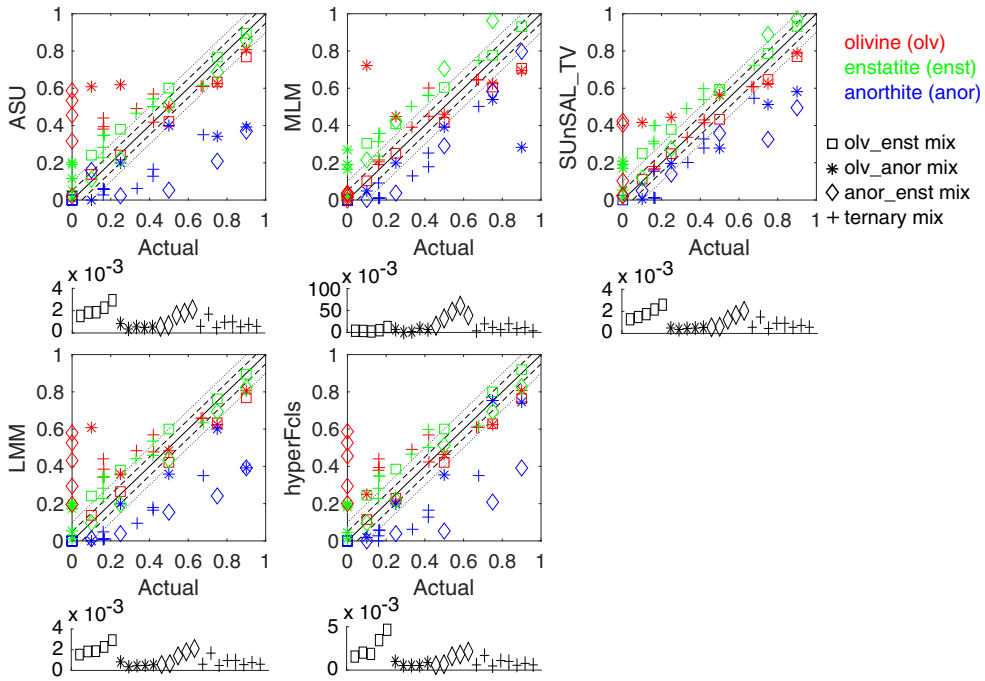

Fig. 5. Volume abundance estimates from five unmixing programs applied to the Hapke transformed SSA CRISM FRT MP89 spectra together with the RELAB Mafic 272 endmember library trimmed to the 14 spectra that were selected most commonly by the five unmixing algorithms when unmixing using the full 272 endmember spectral library, compared to the actual mineral volume abundance values for each mixture in the MP89 data set. Red = olivine (olv), green = enstatite/orthopyroxene (enst), blue = anorthite/plagioclase (anor), and squares = olv + enst mixture, asterisks = olv + anor mixture, diamonds = anor + enst mixture, plus signs = ternary mix of olv + enst + anor. Solid, dashed, and dotted lines represent a one-to-one fit, a 5% error, and a 10% error in volume abundance estimation, respectively. Under each abundance plot are the associated RMSE results comparing the input SSA spectra to those reconstructed from the input endmembers and the estimated abundance results from the relevant unmixing program. The *x*-axis represents the 23 spectra in the MP89 data set in the order listed in the caption for Fig. 1 with the symbols again representing the mixture type as in the associated volume abundance plots. (Color figure can be viewed at wileyonlinelibrary.com.)

The resulting abundances were of lower accuracy than those using the actual endmembers collected in the laboratory, with a maximum error from ASU and LMM of 13%, from hyperFcls and hyperFclsMatlab of 12%, from SUnSAL_TV of 11%, and from MLM of 8%. The results from all six programs show the same general trend with an overestimation of the enstatite and an underestimation of the anorthite. In all cases, the abundance errors in nearly every mixture can be reduced if the mass fraction transformation is not applied and the algorithm output abundance is instead used. Using the algorithm output abundances rather than the volume abundances results in no systematic trend in over- or underestimation for any of the three minerals by any of the unmixing programs (Fig. 7) and lower abundance errors. This is due to the SISAL endmembers not being directly linked to physical samples and only being "true" within the spectral space used to calculate them. It therefore makes no physical sense to assign particle densities to them as they are not related to anything with this measurable variable. The RMSE values of the reconstructed spectra range from 2.22×10^{-4} to 2.62×10^{-3} for all algorithms except MLM that ranges from 2.65×10^{-4} to 1.28×10^{-2}, and SUnSAL_TV that ranges from 2.19×10^{-4} to 2.13×10^{-3} (Fig. 7).

Assuming more than three endmembers present in the SISAL extraction returned unrealistic spectra with at least one having SSA values above 1. No unmixing was attempted with these results as it would be impossible to assign a physical reality to them.

Use of Extracted Endmembers to Trim Laboratory Library

While the SISAL-extracted endmembers are not directly linked to the physical endmembers, they could be used to trim the laboratory library by looking for spectra that closely match the SISAL endmembers. This was attempted using both the spectral library that did not contain the actual endmembers (272 spectra) and the spectral library that did (275 spectra). In order to select the optimum endmembers for use in the unmixing

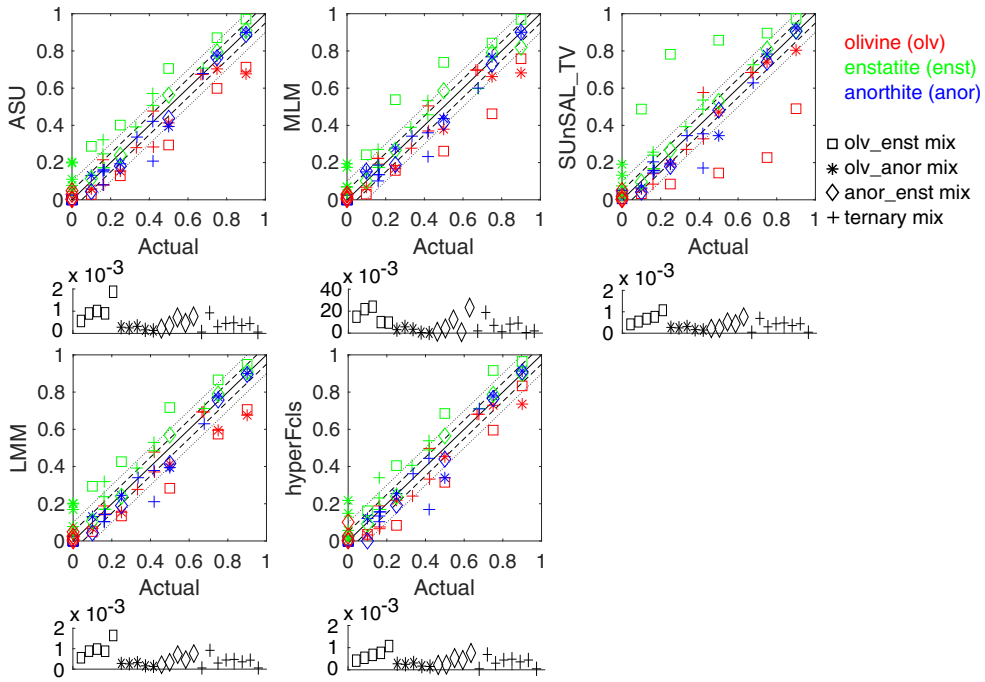

Fig. 6. Volume abundance estimates from five unmixing programs applied to the Hapke transformed SSA CRISM FRT MP89 spectra together with the RELAB Mafic 275 endmember library trimmed to the 27 spectra that were most commonly selected by the five unmixing programs when unmixing using the full 275 endmember spectral library, compared to the actual mineral volume abundance values for each mixture in the MP89 data set. Red = olivine (olv), green = enstatite/orthopyroxene (enst), blue = anorthite/plagioclase (anor), and squares = olv + enst mixture, asterisks = olv + anor mixture, diamonds = anor + enst mixture, plus signs = ternary mix of olv + enst + anor. Solid, dashed, and dotted lines represent a one-to-one fit, a 5% error, and a 10% error in volume abundance estimation, respectively. Under each abundance plot are the associated RMSE results comparing the input SSA spectra to those reconstructed from the input endmembers and the estimated abundance results from the relevant unmixing program. The *x*-axis represents the 23 spectra in the MP89 data set in the order listed in the caption for Fig. 1 with the symbols again representing the mixture type as in the associated volume abundance plots. (Color figure can be viewed at wileyonlinelibrary.com.)

process, SAM values were calculated for each of the three extracted SISAL endmembers against each RELAB spectrum in the 272 and 275 member mafic spectral libraries. The spectra that returned the lowest five SAM values for each of the three SISAL endmembers were selected and further assessed using a visual inspection, removing any that deviated significantly from the relevant SISAL endmember. When the actual endmembers were present, the lowest SAM value for each SISAL endmember match corresponded to one of them. When the actual endmembers were not present, the lowest SAM value for each of the three SISAL extracted endmembers did correspond to an enstatite, an anorthite heavy plagioclase, and an olivine endmember, respectively, the correct three mineral types present in the MP89 mixture data set. This left 13 spectra from the 272 library and 14 spectra from the 275 library. In both cases, the results from the five unmixing programs were all different, again reflecting the nonunique nature of the least squares problem. When the actual endmembers were not present, the maximum abundance error of 38% was returned by the MLM algorithm, the other five returned maximum errors between 24% and 27% (Fig. 8). This maximum error was returned for the same mixture in every case; the mixture with 68% enstatite, 16% anorthite, and 16% olivine. The ASU, LMM, hyperFcls, hyperFclsMatlab, and SUnSAL_TV algorithms in the majority of cases overestimated the abundance of enstatite/orthopyroxene and underestimated the abundance of both olivine and anorthite/plagioclase. The results from MLM showed a different pattern with enstatite/orthopyroxene being overestimated when <40% was present but underestimated when it accounted for a larger percentage of the mixture, olivine was consistently underestimated, and anorthite/plagioclase was generally overestimated when it was present at <50% but estimated within 5% when it was the predominant mineral in the mixture. The RMSE values for ASU and LMM are all similar ranging from 3.23×10^{-4} to 1.09×10^{-2}. RMSE values for hyperFcls are slightly larger ranging 3.72×10^{-4}–1.33×10^{-2} and largest for MLM ranging 4.09×10^{-4}–5.51×10^{-2}. The lowest RMSE values come from SUnSAL_TV ranging

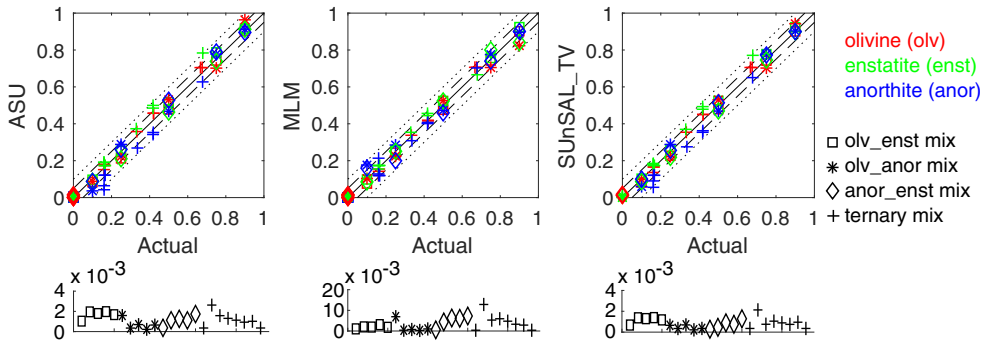

Fig. 7. Abundance estimates (prior to applying the mass fraction transformation) from three unmixing programs applied to the Hapke transformed SSA CRISM FRT MP89 spectra together with the three endmembers extracted using SISAL, compared to the actual mineral volume abundance values for each mixture in the MP89 data set. Red = olivine (olv), green = enstatite (enst), blue = anorthite (anor), and squares = olv + enst mixture, asterisks = olv + anor mixture, diamonds = anor + enst mixture, plus signs = ternary mix of olv + enst + anor. Solid, dashed, and dotted lines represent a one-to-one fit, a 5% error, and a 10% error in abundance estimation, respectively. The results for the unmixing programs LMM, hyperFcls and hyperFclsMatlab were all identical to those for ASU and are not shown here. Under each abundance plot are the associated RMSE results comparing the input SSA spectra to those reconstructed from the input endmembers and the estimated abundance results from the relevant unmixing program. The *x*-axis represents the 23 spectra in the MP89 data set in the order listed in the caption for Fig. 1 with the symbols again representing the mixture type as in the associated abundance plots. (Color figure can be viewed at wileyonlinelibrary.com.)

3.23×10^{-4}–8.02×10^{-3} (Fig. 8). The addition of the actual MP89 endmember spectra to the initial endmember library improved the results. When the trimmed 275 library was used, ASU, hyperFcls, LMM, and SUnSAL_TV return similar but not identical abundances with a maximum error of 10% in all four cases (Fig. 9). MLM returns a much higher maximum error of 21% and a slight tendency to overestimate the abundance of anorthite/plagioclase and underestimate the presence of enstatite/orthopyroxene. The RMSE values reflect these variations in abundance error with MLM returning the highest values ranging from 4.16×10^{-4} to 1.66×10^{-2} and ASU, hyperFcls, and LMM returning ranges of 7.44×10^{-5}–1.91×10^{-3}. The lowest RMSE values are from the SUnSAL_TV results ranging 6.43×10^{-5}–1.45×10^{-3} (Fig. 9).

Martian Shergottites—Spectrally Neutral and Minor Additional Endmembers

The 19 shergottite spectra and 8 shergottite bulk mineralogies show some clear variations (see Fig. 2; Table 1). Where more than one bulk mineralogy study has been performed, the specificity of the minerals identified varies as does the amount of each. QUE 94201 is a clear example of the pyroxene being identified in one study simply as pyroxene, being listed as clinopyroxene in another, and as a quantified mixture of pigeonite and augite in the third. The bulk mineralogy results for Y-984028 are all from the same study that looked at three different subsamples of the meteorite and reports significantly different abundances of the bulk minerals for each. The metadata accompanying the shergottite spectra in the RELAB database do not specify the subsample used in the spectra collection and thus pairing them confidently to one particular bulk mineralogy composition is not possible. The average bulk mineralogy values over those listed in Table 1 are taken as the comparison values for assessing the unmixing abundance estimates with the caveat that in some cases, the error in estimate that would be within the allowable range is considerable.

The spectra show variations both between the different meteorites and within the meteorites where there is more than one spectra collected (Fig. 2). All are dominated by the presence of pyroxene and/or olivine with major absorption bands around 1 μm and 2–2.1 μm with the exact location of these bands varying due to differences in mineralogy between meteorites and between different samples of the same meteorite. The average and peak reflectance also show variation across spectra from the same meteorite even when the absorptions are in the same locations. The two lithologies of EETA 79001 are clearly evident in the shift of the longer wavelength pyroxene absorption from 1.99 μm to 2.09 μm, and in the 1 micron band from 0.95 to 0.97 μm from lithology A to lithology B. Both of these absorption band shifts are due to the difference in bulk mineralogy between these two lithologies (see Table 1) with lithology A containing olivine and small amounts of orthopyroxene, both of which are absent in lithology B (McSween and Jarosewich 1983). Despite the samples being prepared in a similar fashion, all 19 spectra show a much lower average reflectance in

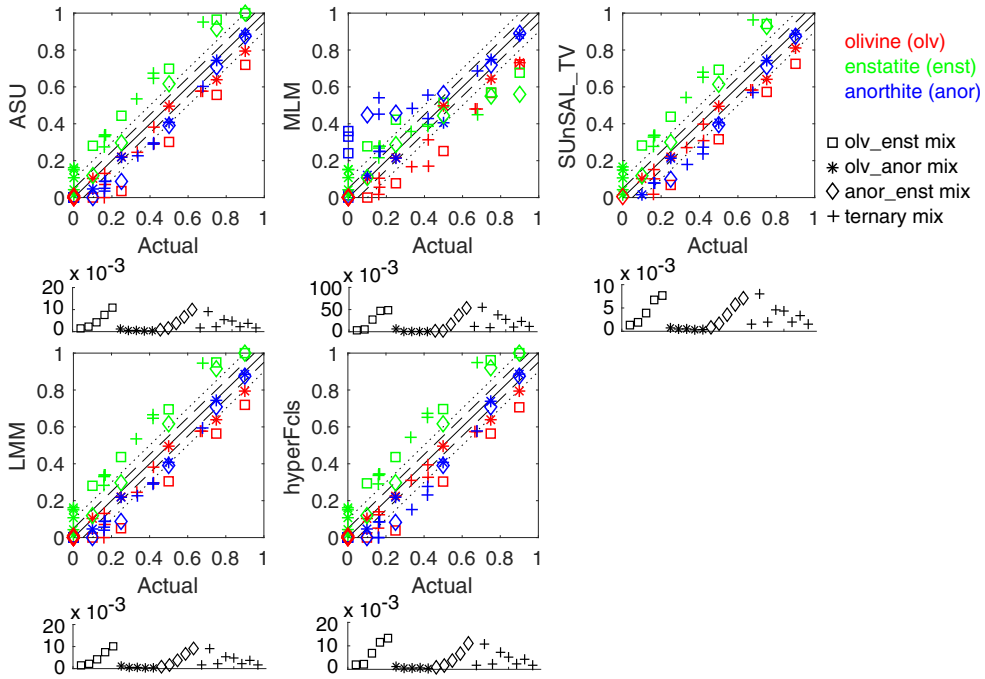

Fig. 8. Volume abundance estimates from five unmixing programs applied to the Hapke transformed SSA CRISM FRT MP89 spectra together with the RELAB Mafic 272 endmember library trimmed to those that most closely match the three endmember spectra extracted by SISAL, compared to the actual mineral volume abundance values for each mixture in the MP89 data set. Red = olivine (olv), green = enstatite/orthopyroxene (enst), blue = anorthite/plagioclase (anor), and squares = olv + enst mixture, asterisks = olv + anor mixture, diamonds = anor + enst mixture, plus signs = ternary mix of olv + enst + anor. Solid, dashed, and dotted lines represent a one-to-one fit, a 5% error, and a 10% error in volume abundance estimation, respectively. Under each abundance plot are the associated RMSE results comparing the input SSA spectra to those reconstructed from the input endmembers and the estimated abundance results from the relevant unmixing program. The *x*-axis represents the 23 spectra in the MP89 data set in the order listed in the caption for Fig. 1 with the symbols again representing the mixture type as in the associated volume abundance plots. (Color figure can be viewed at wileyonlinelibrary.com.)

comparison to the MP89 data set, likely due to the significant presence of glasses and mesostasis materials that have low albedo reflectance spectra (Farrand et al. 2016; Cannon et al. 2017).

The actual endmember mineral spectra for each meteorite were not all available and so a laboratory library was needed. The RELAB mafic library used to unmix the MP89 data set was supplemented with spectra from clinopyroxene samples as well as glasses, impact melts, maskelynites, and mafic minerals altered by radiation and heat resulting in an endmember library of 610 spectra. Additional spectra to represent the minor minerals potentially present in some of the meteorite samples were not included as these would be minor constituents amounting to less than 5% abundance in the majority of cases. Only Los Angeles, QUE 94021, and Y-984028 contain more than this abundance of total additional minerals and for each of these meteorites, this fraction of the bulk is comprised of multiple different minerals. This library was greater in number than the number of spectral bands in the shergottite spectra which were resampled to CRISM FRT resolution. For this reason, the hyperFcls, hyperFclsMatlab, and ASU programs did not return realistic results and were not considered for the rest of this experiment.

Laboratory Library Trimmed by Occurrence

The 610 endmember library was trimmed in a similar manner to the Use of Massive Laboratory Library section, removing all endmembers that do not appear in at least two of the three programs at least once with a value of at least 1% until no more could be removed resulting in a final endmember set of 178 spectra. This library trimming method resulted in a larger endmember library than for the MP89 data set but there are expected to be many more endmembers present in the shergottite data set. The RMSE values for all three program reconstructions have a minimum value of 2.53×10^{-4} and maximum values of 1.64×10^{-3} for SUnSAL_TV, 2.33×10^{-3} for LMM, and 1.52×10^{-1} for MLM (Fig. 10). The abundance estimates from the three algorithms used are all different with a maximum error of 49% (Fig. 10). LEW

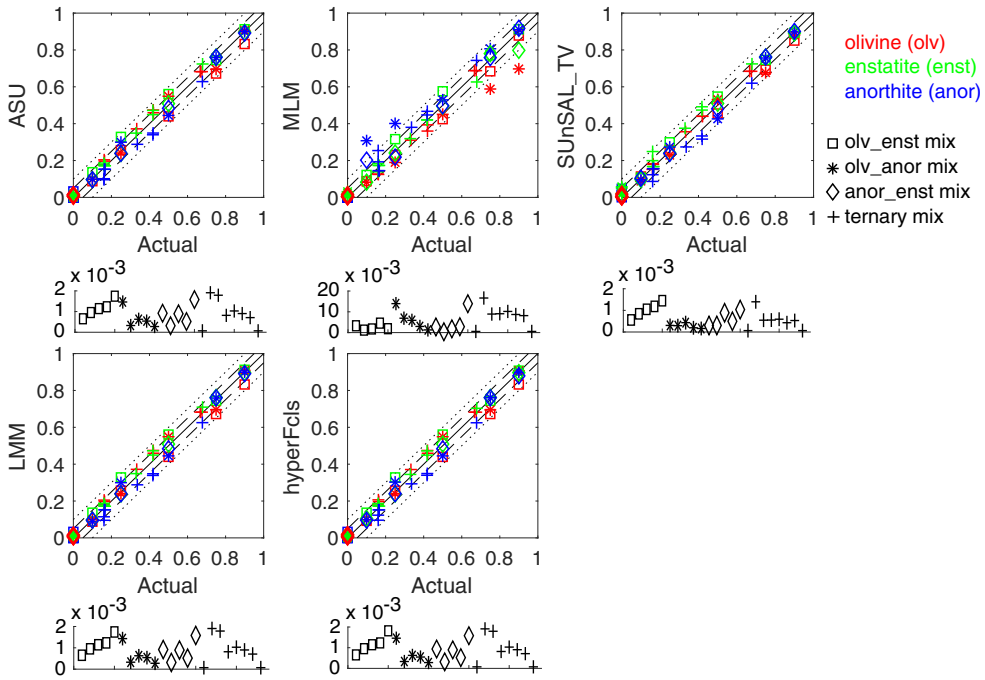

Fig. 9. Volume abundance estimates from five unmixing programs applied to the Hapke transformed SSA CRISM FRT MP89 spectra together with the RELAB Mafic 275 endmember library trimmed to those that most closely match the three endmember spectra extracted by SISAL, compared to the actual mineral volume abundance values for each mixture in the MP89 data set. Red = olivine (olv), green a = enstatite/orthopyroxene (enst), blue = anorthite/plagioclase (anor), and squares = olv + enst mixture, asterisks = olv + anor mixture, diamonds = anor + enst mixture, plus signs = ternary mixture of olv + enst + anor mixture. Solid, dashed, and dotted lines represent a one-to-one fit, a 5% error, and a 10% error in volume abundance estimation, respectively. Under each abundance plot are the RMSE results comparing the input SSA spectra to those reconstructed from the input endmembers and the estimated abundance results from the relevant unmixing algorithm. The *x*-axis represents the 23 spectra in the MP89 data set in the order listed in the caption for Fig. 1 with the symbols again representing the mixture type as in the associated volume abundance plots. (Color figure can be viewed at wileyonlinelibrary.com.)

88517 and Los Angeles return the highest errors in all three programs, overestimating the pyroxene and underestimating the olivine and maskelynite, respectively.

Laboratory Library Trimmed by SISAL Matches

We also use SISAL to extract endmembers. In this case, the precise number of endmembers to extract was unclear. While all shergottites are composed of the same major mineral types, the exact chemical composition and thus spectral endmember of each of these constituent minerals are not guaranteed to be the same for each meteorite sample. The spread of wavelength values of the two major absorptions suggests at least three pyroxenes and at least two plagioclase/maskelynite endmembers are present. It was decided to extract five and nine endmembers. Fewer than five would not cover all the variation and more than nine when there are only 19 spectra in the input data set would start to just return the input spectra. In both cases, all of the extracted spectra looked realistic with no albedo greater than one or unusual looking reflectance peaks rather than absorption troughs. The five-member extracted data set contained two spectra that had the characteristics of olivine (an absorption around 1.05 μm and no 2 μm absorption) and three with the major absorption features of pyroxene signatures. The nine-member data set extracted two spectra that matched general olivine spectral signatures with the other seven all having both a 1 and 2 μm absorption band matching the general shape of pyroxene spectra. Neither of the data sets contain an endmember that could obviously represent the spectrally neutral signatures of glass, melt, or most plagioclase minerals. SAM values were calculated for each extracted endmember in each data set against the 610 RELAB laboratory spectral endmember library. The top-five matches for each extracted SISAL endmember was collected and visually inspected to gauge the match. RELAB spectra that visually deviated from the major spectral features of the extracted endmember were discarded. The final endmember data sets contained 21 endmembers for the SISAL5 extraction and 32 for the SISAL9 extraction.

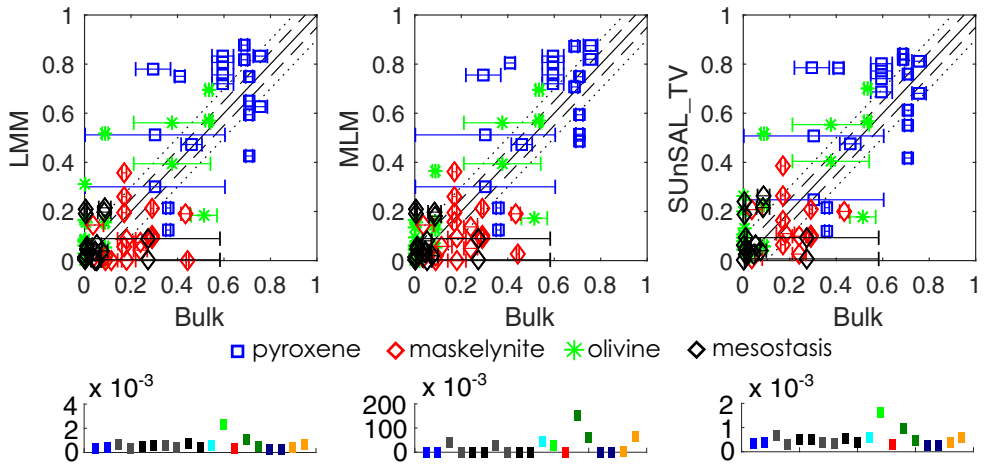

Fig. 10. Volume abundance estimates from three unmixing programs applied to the shergottite spectral data set using the extended RELAB Mafic endmembers library trimmed to the spectra that were most commonly selected when the unmixing was performed using the full endmember library, plotted against the actual bulk mineralogy abundance values taken as the average of the values in Table 1. Blue squares = pyroxene, red diamonds = maskelynite, green asterisks = olivine, and black diamonds = mesostasis. The horizontal error bars represent the spread in the reported bulk mineralogy values in Table 1. Solid, dashed, and dotted lines represent a one-to-one fit, a 5% error, and a 10% error in volume abundance estimation, respectively. Under each abundance plot are the associated RMSE results comparing the input SSA spectra to those reconstructed from the input endmembers and the estimated abundance results from the relevant unmixing program. The *x*-axis represents the 19 spectra in the shergottite data set in the order listed in the caption for Fig. 2 with the colors representing the meteorite subtype as in Fig. 2 where blues = intermediate ultramafic poikilitic, grays/blacks = intermediate permafic olivine-phyric and mafic, greens = enriched mafic diabasic, reds = depleted mafic diabasic, and yellows = enriched mafic intersertal. (Color figure can be viewed at wileyonlinelibrary.com.)

Both data sets contained a maskelynite spectrum taken from EETA 79001 and a number of other pyroxene and olivine spectra taken from meteorites. The EETA 79001 maskelynite is the only plagioclase spectra in the SISAL5 endmember data set and one of only two plagioclase spectra in the SISAL9 endmember data set, the other being a shocked plagioclase spectra. The SISAL5 matched data set contains no glasses but one meteorite impact melt. The SISAL9 matched data set contains a lunar impact melt and one glass from EETA 79001A. The reconstructions from the unmixing results using both the SISAL-matched data sets show deviations from the original input SSA spectra suggesting the endmember library did not contain all of the necessary spectral features of the meteorite spectra. The reconstructions from SUnSAL_TV are the closest match visually in both cases but do include some errors where the absorption peak is slightly shifted. The MLM reconstructions are the poorest and the LMM reconstructions are also wavelength shifted where they do not match well. The RMSE values reflect this with the MLM returning the maximum values for both SISAL5-matched data set and SISAL9-matched data set, 8.85×10^{-2} and 9.28×10^{-2}, respectively (Figs. 11 and 12). The maximum values for SISAL5 for LMM and SUnSAL_TV are 1.36×10^{-2} and 8.40×10^{-3}, respectively, and for SISAL9 they are 1.32×10^{-2} and 6.47×10^{-3}. The minimum values are lower for SISAL9 compared to the SISAL5 minimum values. The minimum RMSE values for the SISAL5-matched reconstructions are 1.43×10^{-3} for LMM, 1.34×10^{-3} for SUnSAL_TV, and 3.32×10^{-3} for MLM. The minimum RMSE values for SISAL9-matched reconstructions are 8.98×10^{-4} for SUnSAL_TV, 9.002×10^{-4} for LMM, and 2.20×10^{-3} for MLM.

The abundance estimates for the SISAL5-matched endmember data set are different for each of the three unmixing programs (Fig. 11). The highest abundance error is returned by SUnSAL_TV with an overestimate of 68% of pyroxene for one of the Y-984028 spectra; however, the bulk mineralogy for this meteorite is reported with a large variation of results and given that the pyroxene estimate may only be an overestimate of 26%. This spectrum returns the highest abundance error for MLM and LMM as well. The melt/mesostasis bulk abundance estimate from all three programs is either within 5% of the bulk abundance reported in the literature or, when a larger error than 5% is returned it is always an overestimate as opposed to an underestimate of the average literature reported value.

The abundance estimates for the SISAL9 matched endmember data set are also different for all three programs and different from the SISAL5-matched

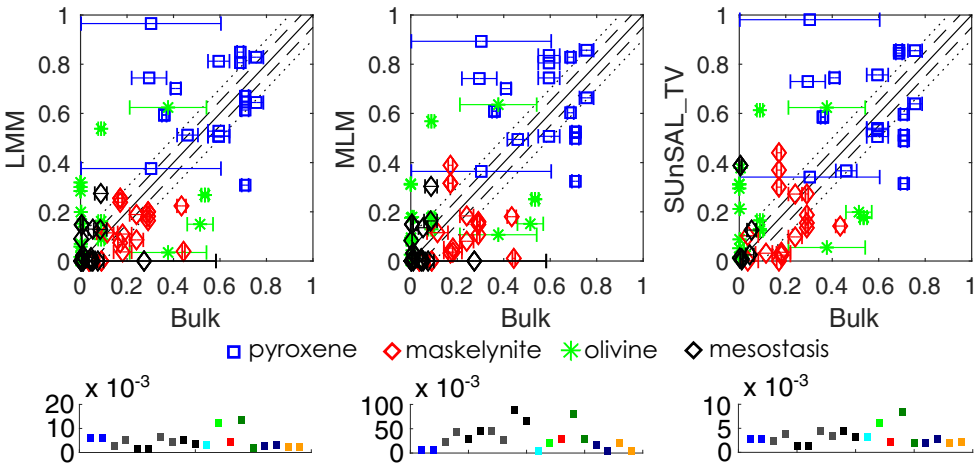

Fig. 11. Volume abundance estimates from three unmixing programs applied to the shergottite spectral data set using the extended RELAB Mafic endmembers library trimmed to those that most closely match the endmembers extracted using the SISAL algorithm set to extract only five endmembers, plotted against the actual bulk mineralogy abundance values taken as the average of the values in Table 1. Blue squares = pyroxene, red diamonds = maskelynite, green asterisks = olivine and black diamonds = mesostasis. The horizontal error bars represent the spread in the reported bulk mineralogy values in Table 1. Solid, dashed, and dotted lines represent a one-to-one fit, a 5% error, and a 10% error in volume abundance estimation, respectively. Under each abundance plot are the associated RMSE results comparing the input SSA spectra to those reconstructed from the input endmembers and the estimated abundance results from the relevant unmixing program. The *x*-axis represents the 19 spectra in the shergottite data set in the order listed in the caption for Fig. 2 with the colors representing the meteorite subtype as in Fig. 2 where blues = intermediate ultramafic poikilitic, grays/blacks = intermediate permafic olivine-phyric and mafic, greens = enriched mafic diabasic, reds = depleted mafic diabasic, and yellows = enriched mafic intersertal. (Color figure can be viewed at wileyonlinelibrary.com.)

results (Fig. 12). The maskelynite is generally underestimated except for three of the four EETA 79001A spectra and both Y-984028 spectra where it is overestimated twice by SUnSAL_TV and MLM and once by LMM. Zagami and Shergotty both have no olivine in the bulk analysis and QUE 94201 has only trace amounts yet unmixing results for all five spectra from these three meteorites return some olivine in at least two of the unmixing program estimates, from as little as 3% to as much as 21%. For the meteorites, where there is more than one spectra being unmixed the results can be varied. The overestimation of pyroxene in ALHA77004 for example ranges from 9 to 45%. Common errors include overestimating olivine, while underestimating both pyroxene and melt/maskelynite, and overestimating pyroxene and underestimating maskelynite.

DISCUSSION

Unmixing Algorithms and Programs

Six different implementations of the linear unmixing model were tested through this work. When the actual mixture spectral endmembers were known and uniquely used as the input endmembers, the codes based on the same fully constrained linear least squared algorithm (hyperFcls, hyperFclsMatlab, LMM, and ASU), all returned the same results. These results are all in agreement with previous works investigating the unmixing of the MP89 data set (e.g., Mustard and Pieters 1987a, 1989). MLM and SUnSAL_TV (based on different algorithms both from each other and the other four programs), however, returned slightly different results. Even in the simple case considered with the MP89 data set, having only three potential endmembers, the unmixing is still a nonunique problem with multiple potential answers from a minimization routine, although the differences between the abundance estimates from the six unmixing programs are small (not more than 2% difference in all but one case where MLM returns errors as high as 11%). In the more complex case where the actual endmembers are unknown and a larger endmember library must be used to ensure full coverage of the potential spectral variability present, the nonunique solution issue is more evident with all six programs returning different results from each other even when based on the same unmixing algorithm. No one program appeared to return consistently more accurate results than the others in either the simple cases with known a priori endmembers, or for different mineral combinations, or the more complex cases using multiple unknown

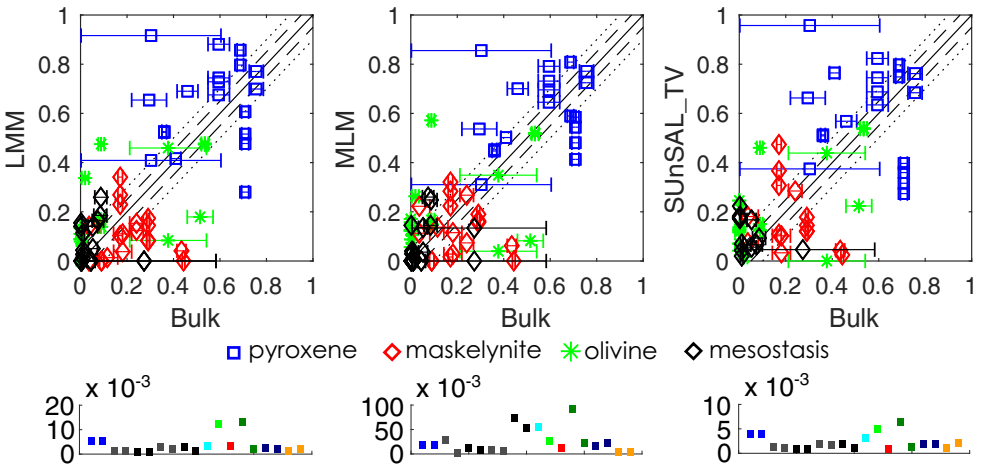

Fig. 12. Volume abundance estimates from three unmixing programs applied to the shergottite spectral data set using the extended RELAB Mafic endmembers library trimmed to those that most closely match the endmembers extracted using the SISAL algorithm set to extract only nine endmembers, plotted against the actual bulk mineralogy abundance values taken as the average of the values in Table 1. Blue squares = pyroxene, red diamonds = maskelynite, green asterisks = olivine, and black diamonds = mesostasis. The horizontal error bars represent the spread in the reported bulk mineralogy values in Table 1. Solid, dashed, and dotted lines represent a one-to-one fit, a 5% error, and a 10% error in volume abundance estimation, respectively. Under each abundance plot are the associated RMSE results comparing the input SSA spectra to those reconstructed from the input endmembers and the estimated abundance results from the relevant unmixing program. The *x*-axis represents the 19 spectra in the shergottite data set in the order listed in the caption for Fig. 2 with the colors representing the meteorite subtype as in Fig. 2 where blues = intermediate ultramafic poikilitic, grays/blacks = intermediate permafic olivine-phyric and mafic, greens = enriched mafic diabasic, reds = depleted mafic diabasic, and yellows = enriched mafic intersertal. (Color figure can be viewed at wileyonlinelibrary.com.)

endmembers and additional minor constituents. This use of multiple unmixing programs can be used as a method of gauging the accuracy of the results and the level of uniqueness of the problem. The most accurate results in this work (i.e., the MP89 baseline experiment) show the lowest level of variation between the different programs and algorithms.

Data Set Differences—Noise and Contrast

Three of the tests performed were specifically aimed at gauging how well the Hapke linear unmixing pipeline would work on poorer spectral data due to instrument noise, decreased spectral resolution, and decreased spectral contrast, respectively. Taking typical parameters from the CRISM instrument, it was found that neither increased instrument noise nor decreased spectral resolution had a significant impact on the accuracy of the abundance estimation with increased errors of only 1–2%.

The decrease in spectral contrast to mimic surface data returned by satellite instruments, however, showed that spectral contrast is a key factor in the utility of the Hapke unmixing technique. Lowering the spectral contrast of the laboratory data to a level typically observed in CRISM imagery via the addition of a low reflectance flat endmember resulted in significantly less accurate abundance estimation values. The highest errors were seen for mixtures that incorporated high abundances of anorthite, the endmember with the lowest spectral contrast of the three minerals involved. For the binary mixtures that did not include any anorthite, it was consistently selected, which was not the pattern seen in the baseline case. Adding the anorthite endmember to the other two leads to shallower absorption troughs evident in the lower contrast data set which appears to be why the programs were selecting it. In the baseline case, the only endmember that was consistently estimated erroneously was the anorthite in the ternary mixtures where it was underestimated, as a low-contrast endmember, it was presumably not considered by the unmixing programs to be adding much to the mixtures. These findings lend weight to the conclusion that it is the lower spectral contrast that leads to the increase in errors in the Decreased Spectral Contrast to Mimic Average Spectrum from Martian Surface section rather than the addition of the fourth neutral endmember. The presence of minerals with low spectral contrast including maskelynite, glass, and impact melts is expected to have contributed to the uneven abundance estimation results from the shergottite data set. Further laboratory tests could be undertaken to validate these results using VNIR spectra collected under conditions that could

return lower spectral contrast from mixtures re-creating those of the MP89 data set, e.g., under low lighting conditions, thereby creating a low spectral contrast data set with known endmembers and abundances without the need for a scaling endmember.

Low spectral contrast is a well-understood issue for users of CRISM data. A common technique to work around this inherent problem is spectral ratioing (e.g., Ehlmann et al. 2008; Skok et al. 2010). Spectral ratioing involves identifying a spectrally neutral pixel and using it as a denominator in a ratio with a pixel of interest that is thought to contain a weak spectral feature of interest. In this way the feature of interest is enhanced enabling a more confident identification of the mineral responsible. While this does enhance spectral bands that are not present in the "neutral" pixel, it also removes the general shape of the spectrum and the contribution of the general background mineralogy, which is presumably present in both pixels. For this reason spectral ratioing can be used to qualitatively identify minerals that are present in discrete amounts in localized regions but cannot be used for quantitative evaluation of the more general planetary surface or for investigating large regions at a time. The low spectral contrast of satellite spectral imagery would appear to be an impediment to quantitative analysis where minerals with low spectral contrast comprise a significant portion of the surface mineralogy (roughly >25%).

Unknown Endmembers—Spectra and Minerals

In an exploration situation, it is highly unlikely that the precise spectral endmembers present will be known. To enable the mixture spectra to be unmixed and ensure that all spectral features are available to the unmixing routine, more endmembers than are present will most likely need to be supplied (Combe et al. 2008; Li et al. 2015). This larger endmember set could still include the actual endmembers present in the mixtures but even in this case (see the Unknown Spectral Endmembers section), the addition of the extra endmembers that are not actually present leads to a decrease in abundance estimation accuracy. This was found to be the case even when using the SUnSAL_TV algorithm, a sparse unmixing algorithm specifically designed to be used in cases where there are more input unmixing endmembers than exist in the mixture data set (Iordache et al. 2012). Even when the actual endmembers are present, the larger the number of endmembers used, the larger the errors in the abundance estimation. It is therefore expedient to use as small an endmember data set as possible.

Two methods for selecting the optimal endmember library (balancing total number of endmembers against covering the full spectral and mineral diversity suspected to be present) were investigated. Making use of multiple unmixing programs allowed the use of a basic trimming method keeping only those endmembers that were commonly selected across the programs, a similar method to that used by Li and Milliken (2015) in their work investigating the use of Hapke transformation and linear unmixing applied to the HED meteorites. The unmixing programs predominantly selected the correct mineral types (e.g., selecting anorthite-rich plagioclase samples for the MP89 data set analyses) but unless the actual endmembers were present the trimming of the endmember library via common occurrence did not improve the abundance results. For the MP89 data set, it was found that using these trimmed input endmember data sets resulted in frequent overestimation of enstatite/orthopyroxene and olivine and underestimation of anorthite/plagioclase when the actual endmember spectra were not present. When the actual endmembers were present, the common pattern was to overestimate the enstatite/orthopyroxene and underestimate the olivine and anorthite/plagioclase. Anorthite/plagioclase is the endmember with the flattest spectral signature of the three minerals present, and this is likely to contribute to its underestimation in all cases. The primary absorption feature of olivine is a broad absorption band centered at around 1 μm (Sunshine and Pieters 1998). Orthopyroxenes also have a major absorption feature around this wavelength (Sunshine et al. 1990). Given that the overestimation of enstatite/orthopyroxene in the experiments presented here is correlated with an underestimation of olivine when the actual endmembers are not present it would appear that this is the likely cause for the discrepancy. Olivine and orthopyroxene commonly co-occur within Martian meteorites (Lodders 1998) and on the Martian surface (McSween 2015) and it is therefore important to be able to accurately discriminate between the two mineral species. Underestimation of the amount of olivine present in CRISM images could have far-reaching implications for interpretation of the evolution of the Martian surface as olivine in high abundances could mean that little aqueous alteration has occurred (e.g., Koeppen and Hamilton 2008).

A second method utilizing endmember extraction algorithms (EEAs) was considered. A suitable EEA needs to be able to cope with intimate nonlinear mixtures and a lack of "pure" spectra in the mixture data set. Few EEAs are openly available that meet these criteria and come with their own issues. SISAL was used in this work but it is known to struggle with the identification and extraction of low spectral contrast endmembers (Harris 2016). Additionally, the spectral endmembers that are extracted are not directly linked to the underlying physical reality of the endmember

mineral grains. This makes them inappropriate for Hapke unmixing as physical characteristics such as density cannot be applied to these extracted spectra. A secondary use of these extracted spectra was investigated, if they could be mapped to laboratory reflectance spectra thereby giving them a physical reality that could be used in the Hapke unmixing routine. When using the MP89 data set extracted, spectra did match well to the correct mineral types and when the actual mixture endmembers were included in the potential matching library, they were selected as closest matches. SISAL (and other EEAs) requires a priori knowledge of the number of endmembers present. If this piece of information is known, using the SISAL-extracted spectra as proxies to match to spectral library endmembers was a successful method of selecting input endmembers for the unmixing routine if correct endmembers exist in the spectral library in question and all have significant absorption features. However, the difficulty in extracting spectrally neutral endmembers and the need to know the number of endmembers present limits the use of this technique on satellite data and natural mixtures from the Martian surface.

Spectral Reconstruction RMSE and SAM as Proxy for Abundance Estimation Error

A common metric used to assess the accuracy of unmixing results from a data set with unknown endmember abundances is to compare the original mixture spectra to spectra reconstructed from the abundance results and their associated endmember spectra (e.g., Plaza et al. 2011; Goudge et al. 2015). RMSE and SAM are two values that can be calculated to quantify how closely the original and reconstructed spectra match. The nonuniqueness of the unmixing problem as demonstrated in the use of different unmixing programs that are all performing the same least squares minimization using different methods raises doubts as to the validity of this metric. The larger the endmember library used in the unmixing routine, the higher the chance of nonunique solutions. When large endmember libraries were used, it was also found that low RMSE and SAM values could be returned (demonstrating a highly accurate match between the input and reconstructed mixture spectra) for abundances that deviated by tens of percent from the correct abundances (see Figs. 5 and 6). How well the reconstructed spectra match to the original spectra is not therefore a reliable measure of the accuracy of the abundance estimation, with the higher the number of excess endmembers fed into the unmixing routine, the higher the level of potential false positives within the problem and thus the higher the number of incorrect solutions. As per the Unknown Endmembers—Spectra and Minerals section, limiting the number of input unmixing endmembers is therefore a key issue in the use of spectral unmixing routines.

Natural Rock Powders Versus Synthetic Mixtures

The MP89 data set was created in the laboratory and is a completely synthetic mixture. Mixtures found in the surface regolith of planets are generally much more complex, in terms of number and proportion of constituent minerals and physical characteristics of these minerals. It was this disparity that the shergottite analysis was addressing. The shergottite samples were all powdered to uniform grain size fractions as were the mineral samples used to create MP89 mixture data set. This does not guarantee complete physical homogeneity across the different minerals however and differences in crystal size likely contribute to the 5% abundance estimation errors seen in the binary and ternary synthetic mixtures. In the natural mixtures of the shergottites, the presence of a range of minor constituent minerals besides the major mafic endmembers also appears to have contributed to the higher inaccuracies of the abundance estimation, beyond that which can be explained by the range of bulk mineralogy values reported in previous studies for each meteorite.

Recommendations

This work introduced various simplifications to the Hapke unmixing model to account for unknowns in the face of remotely sensed spectral data. These simplifications do not detract from the accuracy of the method when using high-resolution, high spectral contrast, and high SNR laboratory data for which the spectral signatures of the endmember constituents are known, but when the endmember spectra are unknown or these data are degraded to mimic low spectral contrast satellite data, the results are also degraded. A number of future avenues present themselves as an outcome of these results. First, the use of statistical methods (such as Monte Carlo [Ciarniello et al. 2014; Lapotre et al. 2017]) could be explored to assign probabilities to results, giving a better indication of the potential accuracy of the abundance estimates in the face of numerous false positives and nonunique results. Second, the use of EEAs to estimate the endmembers present could be further investigated concentrating on algorithms that could potentially identify spectrally neutral endmembers when present. Third, future work could attempt to quantify the level of minor constituents such as those that occur in the shergottite samples. These additional minor endmembers are a

ubiquitous feature of the Martian surface (as evidenced by their presence in the vast majority of Martian meteorites) and a method of dealing with their presence is necessary if the mineralogy of the Martian surface is to be accurately quantified from VNIR imagery. Even if these minor minerals cannot be individually identified, having an accurate estimate as to the volume fraction they account for would allow for more accurate estimates of the major bulk minerals. Improving the accuracy of this technique for use with CRISM data in particular would allow a host of outstanding questions about the surface of Mars to be answered, including helping to identify the source craters of the Martian meteorites through matching of meteorite bulk mineralogies to surface abundance values.

CONCLUSIONS

Spectral data collected by a satellite instrument of a planetary surface contain numerous complications compared to spectra from defined mineral mixtures collected under controlled laboratory conditions. We have attempted here to quantify the effect these differences have on the accuracy when using a linear mixture model to unmix reflectance data from mineral mixtures that have been transformed into SSA via the nonlinear Hapke radiative transfer equation. For laboratory data with clearly defined endmembers, this Hapke unmixing routine works well (accuracies within 5% for binary and ternary mixtures), even with the simplifications introduced in this paper to account for the parameters that are frequently unknown and unknowable from satellite data alone. The low spectral contrast of CRISM data, however, appears to present an inherent limitation to the use of this method in quantitatively analyzing the surface of Mars using VNIR spectroscopy, with estimated abundances being accurate to only within 25%. Results presented here suggest caution must be exercised when using VNIR satellite data to deduce mineral abundances from the regolith of Mars.

Acknowledgments—The authors thank the editor, Dr. E. Cloutis, and reviewer, Dr. C. Carli, for helpful comments that improved the quality of this paper. This work was funded by STFC grant ST/R002827/1.

Editorial Handling—Dr. Edward Cloutis

REFERENCES

Antarctic Meteorite Working Group. 1981. *Antarctic Meteorite Newletter vol. 4 no. 2 (NASA)*. https://ntrs.nasa.gov/archive/nasa/casi.ntrs.nasa.gov/19820014254.pdf. Accessed February 22, 2018.

Berman M., Bischof L., Lagerstrom R., Guo Y., Huntington J., Mason P., and Green A. A. 2017. A comparison between three sparse unmixing algorithms using a large library of shortwave infrared mineral spectra. *IEEE Transactions on Geoscience and Remote Sensing* 55:3588–3610.

Bernard-Michel C., Douté S., Fauvel M., Gardes L., and Girard S. 2009. Retrieval of Mars surface physical properties from OMEGA hyperspectral images using regularized sliced inverse regression. *Journal of Geophysical Research* 114:E06005.

Bibring J.-P., Soufflot A., Berthé M., Langevin Y., Gondet B., Drossart P., Bouyé M., and Combes M. 2004. *OMEGA : Observatoire pour la Minéralogie, l 'Eau, les Glaces et l 'Activité*. Paris: European Space Agency.

Bibring J.-P., Langevin Y., Gendrin A., Gondet B., Poulet F., Berthé M., Soufflot A., Arvidson R., Mangold N., Mustard J., Drossart P., and the OMEGA team. 2005. Mars surface diversity as revealed by the OMEGA/Mars Express observations. *Science* 307:1576–1581.

Bibring J.-P., Langevin Y., Mustard J. F., Poulet F., Arvidson R., Gendrin A., Gondet B., Mangold N., Pinet P., Forget F., Berthé M., Bibring J. P., Gendrin A., Gomez C., Gondet B., Jouglet D., Poulet F., Soufflot A., Vincendon M., Combes M., Drossart P., Encrenaz T., Fouchet T., Merchiorri R., Belluci G., Altieri F., Formisano V., Capaccioni F., Cerroni P., Coradini A., Fonti S., Korablev O., Kottsov V., Ignatiev N., Moroz V., Titov D., Zasova L., Loiseau D., Mangold N., Pinet P., Douté S., Schmitt B., Sotin C., Hauber E., Hoffmann H., Jaumann R., Keller U., Arvidson R., Mustard J. F., Duxbury T., Forget F., and Neukum G. 2006. Global mineralogical and aqueous mars history derived from OMEGA/Mars Express data. *Science* 312:400–404.

Bioucas-Dias J. M. B. 2009. A variable splitting augmented Lagrangian approach to linear spectral unmixing. In *2009 First workshop on hyperspectral image and signal processing: Evolution in remote sensing*. New York: IEEE. pp. 1–4

Bioucas-Dias J. M. B., Plaza A., Dobigeon N., Parente M., Du Q., Gader P., and Chanussot J. 2012. Hyperspectral unmixing overview: Geometrical, statistical, and sparse regression-based approaches. *IEEE Journal of Selected Topics in Applied Earth Observations and Remote Sensing* 5:354–379.

Broadwater J., Banerjee A., and Burlina P. 2009. Kernel methods for unmixing hyperspectral imagery. In *Kernal methods for remote sensing data analysis*, edited by Camps-Valls G. and Bruzzone L. New York: John Wiley & Sons. pp. 249–269.

Bultel B., Quantin C., and Lozac'h L. 2015. Description of CoTCAT (Complement to CRISM Analysis Toolkit). *IEEE Journal of Selected Topics in Applied Earth Observations and Remote Sensing* 8:3039–3049.

Burns R. G. 1993. *Mineralogical applications of crystal field theory*, 2nd ed. Cambridge, UK: Cambridge University Press.

Cannon K. M., Mustard J. F., Parman S. W., Sklute E. C., Dyar M. D., and Cooper R. F. 2017. Spectral properties of Martian and other planetary glasses and their detection in remotely sensed data. *Journal of Geophysical Research: Planets* 122:249–268.

Ciarniello M., Capaccioni F., and Filacchione G. 2014. A test of Hapke's model by means of Monte Carlo ray-tracing. *Icarus* 237:293–305.

Clark R. N. 1999. Spectroscopy of rocks and minerals and the principles of spectroscopy. In *Manual of remote sensing, Volume 3, Remote sensing for the earth sciences*, edited by Rencz A. N. New York: John Wiley & Sons. pp. 3–58.

Clark R. N. and Roush T. L. 1984. Reflectance spectroscopy: Quantitative analysis techniques for remote sensing applications. *Journal of Geophysical Research* 89:6329–6340.

Cloutis E. A. 1996. Review article hyperspectral geological remote sensing: Evaluation of analytical techniques. *International Journal of Remote Sensing* 17:2215–2242.

Combe J.-P., Le Mouélic S., Sotin C., Gendrin A., Mustard J. F., Le Deit L., Launeau P., Bibring J.-P., Gondet B., Langevin Y., Pinet P., and the OMEGA Science Team. 2008. Analysis of OMEGA/Mars express data hyperspectral data using a Multiple-Endmember Linear Spectral Unmixing Model (MELSUM): Methodology and first results. *Planetary and Space Science* 56:951–975.

Dobigeon N., Tourneret J.-Y., Richard C., Bermudez J. C. M., McLaughlin S., and Hero A. O. 2014. Nonlinear unmixing of hyperspectral images: Models and algorithms. *IEEE Signal Processing Magazine* 31:82–94.

Duke M. B. 1968. The Shergotty meteorite—Magmatic and shock metamorphic features. In *Shock metamorphism of natural materials*, edited by French B. M. and Short N. M. Baltimore, Maryland: Mono Book Corporation. pp. 613–621.

Ehlmann B. L. and Edwards C. S. 2014. Mineralogy of the Martian surface. *Annual Review of Earth and Planetary Sciences* 42:291–315.

Ehlmann B. L., Mustard J. F., Murchie S. L., Poulet F., Bishop J. L., Brown A. J., Calvin W. M., Clark R. N., Marais D. J., Milliken R. E., Roach L. H., Roush T. L., Swayze G. A., and Wray J. J. 2008. Orbital identification of carbonate-bearing rocks on Mars. *Science* 322:1828–1832.

Farrand W. H., Wright S. P., Rogers A. D., and Glotch T. D. 2016. Basaltic glass formed from hydrovolcanism and impact processes: Characterization and clues for detection of mode of origin from VNIR through MWIR reflectance and emission spectroscopy. *Icarus* 275:16–28.

Gleason J. D., Kring D. A., Hill D. H., and Boynton W. V. 1997. Petrography and bulk chemistry of Martian lherzolite LEW88516. *Geochimica et Cosmochimica Acta* 61:4007–4014.

Goudge T. A., Mustard J. F., Head J. W. III, Salvatore M. R., and Wiseman S. M. 2015. Integrating CRISM and TES hyperspectral data to characterize a halloysite-bearing deposit in Kashira crater, Mars. *Icarus* 250:165–187.

Hapke B. 1981. Bidirectional reflectance spectroscopy: 1. Theory. *Journal of Geophysical Research* 86:3039.

Hapke B. 2012. *Theory of reflectance and emittance spectroscopy*, 2nd ed. Cambridge, UK: Cambridge University Press.

Harris J. K. 2016. *Visible and near infrared imaging spectroscopy and the exploration of small scale hydrothermally altered and hydrated environments on Earth and Mars*. Birkbeck: University of London.

Harris J. K., Cousins C. R., and Claire M. W. 2016. Spectral identification and quantification of salts in the Atacama Desert. In *SPIE 10005, earth resources and environmental remote sensing/GIS applications VII*, edited by Michel U., Schulz K., Ehlers M., Nikolakopoulos K. G., and Civco D. Edinburgh, UK: SPIE. 100050I p.

Harvey R. P., McCoy T. J., and Leshin L. A. 1996. Shergottite QUE 94201: Texture, mineral compositions, and comparison with other basaltic shergottites. In *Proceedings of the Lunar and Planetary Science Conference vol. 27*. Houston, Texas: Lunar and Planetary Institute. p. 497.

Heinz D. C. and Chang C.-I. 2001. Fully constrained least squares linear spectral mixture analysis method for material quantification in hyperspectral imagery. *IEEE Transactions on Geoscience and Remote Sensing* 39:529–545.

Herkenhoff K. E., Squyres S. W., Arvidson R., Bass D. S., Bell J. F. 3rd, Bertelsen P., Cabrol N. A., Gaddis L., Hayes A. G., Hviid S. F., Johnson J. R., Kinch K. M., Madsen M. B., Maki J. N., McLennan S. M., McSween H. Y., Rice J. W. Jr., Sims M., Smith P. H., Soderblom L. A., Spanovich N., Sullivan R., and Wang A. 2004. Textures of the soils and rocks at Gusev Crater from Spirit's Microscopic Imager. *Science* 305:824–826.

Heylen R. and Scheunders P. 2014. Hyperspectral unmixing using an active set algorithm. In *2014 IEEE International Conference on Image Processing (ICIP)*. New York: IEEE. pp. 694–697.

Heylen R. and Scheunders P. 2016. A multilinear mixing model for nonlinear spectral unmixing. *IEEE Transactions on Geoscience and Remote Sensing* 54:240–251.

Heylen R., Parente M., and Gader P. 2014. A review of nonlinear hyperspectral unmixing methods. *IEEE Journal of Selected Topics in Applied Earth Observations and Remote Sensing* 7:1844–1868.

Hunt G. R. and Salisbury J. W. 1970. Visible and near-infrared spectra of minerals and rocks: I Silicate minerals. *Modern Geology* 1:283–300.

International Society of Meteoritics and Planetary Sciences. 2017. Meteoritical Bulletin Database. https://www.lpi.usra.edu/meteor/. Accessed January 1, 2017.

Iordache M.-D., Bioucas-Dias J. M., and Plaza A. 2012. Total variation spatial regularization for sparse hyperspectral unmixing. *IEEE Transactions on Geoscience and Remote Sensing* 50:4484–4502.

Keshava N. and Mustard J. F. 2002. Spectral unmixing. *IEEE Signal Processing Magazine* 19:44–57.

Koeppen W. C. and Hamilton V. E. 2008. Global distribution, composition, and abundance of olivine on the surface of Mars from thermal infrared data. *Journal of Geophysical Research* 113:E05001.

Kreisch C. D., O'Sullivan J. A., Arvidson R. E., Politte D. V., He L., Stein N. T., Finkel J., Guinness E. A., Wolff M. J., and Lapôtre M. G. A. 2017. Regularization of Mars Reconnaissance Orbiter CRISM along-track oversampled hyperspectral imaging observations of Mars. *Icarus* 282:136–151.

Kruse F. A., Lefkoff A. B., Boardman J. W., Heidebrecht K. B., Shapiro A. T., Barloon P. J., and Goetz A. F. H. 1993. The Spectral Image Processing System (SIPS)—Interactive visualization and analysis of imaging spectrometer data. *Remote Sensing of Environment* 44:145–163.

Lapotre M. G. A., Ehlmann B. L., and Minson S. E. 2017. A probabilistic approach to remote compositional analysis of planetary surfaces. *Journal of Geophysical Research: Planets* 122:983–1009.

Li S. and Milliken R. E. 2015. Estimating the modal mineralogy of eucrite and diogenite meteorites using visible-near infrared reflectance spectroscopy. *Meteoritics & Planetary Science* 50:1821–1850.

Li J., Agathos A., Zaharie D., Bioucas-Dias J. M. B., Plaza A., and Li X. 2015. Minimum volume simplex analysis: A fast algorithm for linear hyperspectral unmixing. *IEEE*

Transactions on Geoscience and Remote Sensing 53:5067–5082.

Liu D., Li L., and Sun Y. 2015. An improved radiative transfer model for estimating mineral abundance of immature and mature lunar soils. *Icarus* 253:40–50.

Lodders K. 1998. A survey of shergottite, nakhlite and chassigny meteorites whole-rock compositions. *Meteoritics & Planetary Science* 33:A183–A190.

Lucey P. G. 1998. Model near-infrared optical constants of olivine and pyroxene as a function of iron content. *Journal of Geophysical Research: Planets* 103:1703–1713.

Ma M.-S., Schmitt R. A., and Laul J. C. 1981. Complementary rare earth element patterns in unique achondrites, such as ALHA 77005 and shergottites, and in the earth. Proceedings, 12th Lunar and Planetary Science Conference. pp. 1349–1358.

McCoy T. J., Taylor G. J., and Keil K. 1992. Zagami: Product of a two-stage magmatic history. *Geochimica et Cosmochimica Acta* 56:3571–3582.

McSween H. Y. 2015. Petrology on Mars. *American Mineralogist* 100:2380–2395.

McSween H. Y. and Jarosewich E. 1983. Petrogenesis of the Elephant Moraine A79001 meteorite: Multiple magma pulses on the shergottite parent body. *Geochimica et Cosmochimica Acta* 47:1501–1513.

McSween H. Y. and McLennan S. M. 2014. Mars. In *Treatise on geochemistry*, vol. 2, 2nd ed., edited by Holland H. D. and Turekian K. K. Oxford, UK: Elsevier. pp. 251–300.

Mcsween H. Y., Eisenhour D. D., Taylor L. A., Wadhwa M., and Crozaz G. 1996. QUE94201 shergottite: Crystallization of a Martian basaltic magma. *Geochimica et Cosmochimica Acta* 60:4563–4569.

McSween H. Y., Taylor G. J., and Wyatt M. B. 2009. Elemental composition of the Martian crust. *Science* 324:736–739.

Mikouchi T. 2001. Mineralogical similarities and differences between the Los Angeles basaltic shergottite and the Asuka-881757 lunar mare meteorite. *Antarctic Meteorite Research* 14:1–20.

Mikouchi T., Miyamoto M., and McKay G. A. 1998. Mineralogy of Antarctic basaltic shergottite Queen Alexandra Range 94201: Similarities to Elephant Moraine A79001 (Lithology B) Martian meteorite. *Meteoritics & Planetary Science* 33:181–189.

Murchie S. L., Arvidson R., Bedini P., Beisser K., Bibring J.-P., Bishop J., Boldt J., Cavender P., Choo T., Clancy R. T., Darlington E. H., Des Marais D., Espiritu R., Fort D., Green R., Guinness E., Hayes J., Hash C., Heffernan K., Hemmler J., Heyler G., Humm D., Hutcheson J., Izenberg N., Lee R., Lees J., Lohr D., Malaret E., Martin T., McGovern J. A., McGuire P., Morris R., Mustard J., Pelkey S., Rhodes E., Robinson M., Roush T., Schaefer E., Seagrave G., Seelos F., Silverglate P., Slavney S., Smith M., Shyong W.-J., Strohbehn K., Taylor H., Thompson P., Tossman B., Wirzburger M., and Wolff M. 2007. Compact Reconnaissance Imaging Spectrometer for Mars (CRISM) on Mars Reconnaissance Orbiter (MRO). *Journal of Geophysical Research* 112: https://doi.org/10.1029/2006JE002682.

Murchie S. L., Mustard J. F., Ehlmann B. L., Milliken R. E., Bishop J. L., McKeown N. K., Noe Dobrea E. Z., Seelos F. P., Buczkowski D. L., Wiseman S. M., Arvidson R. E., Wray J. J., Swayze G., Clark R. N., Des Marais D. J., McEwen A. S., and Bibring J.-P. 2009. A synthesis of Martian aqueous mineralogy after 1 Mars year of observations from the Mars Reconnaissance Orbiter. *Journal of Geophysical Research* 114:E00D06.

Mustard J. F. and Pieters C. M. 1987a. Quantitative abundance estimates from bidirectional reflectance measurements. *Journal of Geophysical Research* 92:E617–E626.

Mustard J. F. and Pieters C. M. 1987b. Abundance and distribution of ultramafic microbreccia in Moses Rock dike: Quantitative application of mapping spectroscopy. *Journal of Geophysical Research* 92:10,376–10,390.

Mustard J. F. and Pieters C. M. 1989. Photometric phase functions of common geologic minerals and applications to quantitative analysis of mineral mixture reflectance spectra. *Journal of Geophysical Research* 94:13619.

Nascimento J. M. P. and Bioucas-Dias J. M. B. 2010. Unmixing hyperspectral intimate mixtures. In *Image and signal processing for remote sensing XVI*, edited by Bruzzone L. 78300C p. http://proceedings.spiedigitallibrary.org/proceeding.aspx?articleid=725596. Accessed January 22, 2014.

Nyquist L. E., Bogard D. D., Shih C.-Y., Greshake A., Stöffler D., and Eugster O. 2001. Ages and geologic histories of Martian meteorites. *Space Science Reviews* 96:105–164.

Pelkey S. M., Mustard J. F., Murchie S., Clancy R. T., Wolff M., Smith M., Milliken R., Bibring J.-P., Gendrin A., Poulet F., Langevin Y., and Gondet B. 2007. CRISM multispectral summary products: Parameterizing mineral diversity on Mars from reflectance. *Journal of Geophysical Research* 112. https://doi.org/10.1029/2006JE002831.

Pieters C. M. and Hiroi T. 2004. RELAB (Reflectance Experiment Laboratory): A NASA multiuser spectroscopy facility (abstract #1720). 35th Lunar and Planetary Science Conference. CD-ROM.

Pilorget C., Fernando J., Ehlmann B. L., Schmidt F., and Hiroi T. 2016. Wavelength dependence of scattering properties in the VIS–NIR and links with grain-scale physical and compositional properties. *Icarus* 267:296–314.

Plaza J., Hendrix E. M. T., García I., Martín G., and Plaza A. 2011. On endmember identification in hyperspectral images without pure pixels: A comparison of algorithms. *Journal of Mathematical Imaging and Vision* 42:163–175.

Poulet F., Cuzzi J. N., Cruikshank D. P., Roush T. L., and Dalle Ore C. M. 2002. Comparison between the Shkuratov and Hapke scattering theories for solid planetary surfaces: Application to the surface composition of two centaurs. *Icarus* 160:313–324.

Poulet F., Mangold N., Loizeau D., Bibring J.-P., Langevin Y., Michalski J., and Gondet B. 2008. Abundance of minerals in the phyllosilicate-rich units on Mars. *Astronomy & Astrophysics* 487:L41–L44.

Poulet F., Ehlmann B. L., Mustard J. F., Vincendon M., and Langevin Y. 2010. Modal mineralogy of planetary surfaces from visible and near-infrared spectral data. In *2010 2nd Workshop on hyperspectral image and signal processing: evolution in remote sensing*. New York: IEEE. pp. 1–4.

Quintano C., Fernández-Manso A., Shimabukuro Y. E., and Pereira G. 2012. Spectral unmixing. *International Journal of Remote Sensing* 33:5307–5340.

Riches A. J. V., Liu Y., Day J. M. D., Puchtel I. S., Rumble D., McSween H. Y., Walker R. J., and Taylor L. A. 2011. Petrology and geochemistry of Yamato 984028: A cumulate lherzolitic shergottite with affinities to Y 000027, Y 000047, and Y 000097. *Polar Science* 4:497–514.

Robertson K. M., Milliken R. E., and Li S. 2016. Estimating mineral abundances of clay and gypsum mixtures using

radiative transfer models applied to visible-near infrared reflectance spectra. *Icarus* 277:171–186.
Rubin A. E., Warren P. H., Greenwood J. P., Verish R. S., Leshin L. A., Hervig R. L., Clayton R. N., and Mayeda T. K. 2000. Los Angeles: The most differentiated basaltic Martian meteorite. *Geology* 28:1011.
Schmidt F., Legendre M., and Le Mouélic S. 2014. Minerals detection for hyperspectral images using adapted linear unmixing: LinMin. *Icarus* 237:61–74.
Sklute E. C., Glotch T. D., Piatek J. L., Woerner W. R., Martone A. A., and Kraner M. L. 2015. Optical constants of synthetic potassium, sodium, and hydronium jarosite. *American Mineralogist* 100:1110–1122.
Skok J. R., Mustard J. F., Ehlmann B. L., Milliken R. E., and Murchie S. L. 2010. Silica deposits in the Nili Patera caldera on the Syrtis Major volcanic complex on Mars. *Nature Geoscience* 3:838–841.
Smith J. V. and Hervig R. L. 1979. Shergotty meteorite: Mineralogy, petrography and minor elements. *Meteoritics* 14:121–142.
Stöffler D., Ostertag R., Jammes C., Pfannschmidt G., Gupta P. R. Sen, Simon S. B., Papike J. J., and Beauchamp R. H. 1986. Shock metamorphism and petrography of the Shergotty achondrite. *Geochimica et Cosmochimica Acta* 50:889–903.
Stolper E. and McSween H. Y. 1979. Petrology and origin of the shergottite meteorites. *Geochimica et Cosmochimica Acta* 43:1475–1498.
Sunshine J. M. and Pieters C. M. 1998. Determining the composition of olivine from reflectance spectroscopy. *Journal of Geophysical Research: Planets* 103:13,675–13,688.
Sunshine J. M., Pieters C. M., and Pratt S. F. 1990. Deconvolution of mineral absorption bands—An improved approach. *Journal of Geophysical Research: Solid Earth* 95:6955–6966.
Treiman A. H. and Sutton S. R. 1992. Petrogenesis of the Zagami meteorite: Inferences from synchrotron X-ray (SXRF) microprobe and electron microprobe analyses of pyroxenes. *Geochimica et Cosmochimica Acta* 56:4059–4074.
Treiman A. H., McKay G. A., Bogard D. D., Mittlefehldt D. W., Wang M.-S., Keller L., Lipschutz M. E., Lindstrom M. M., and Garrison D. 1994. Comparison of the LEW88516 and ALHA77005 Martian meteorites: Similar but distinct. *Meteoritics* 29:581–592.
Vincendon M., Langevin Y., Poulet F., Bibring J.-P., and Gondet B. 2007. Recovery of surface reflectance spectra and evaluation of the optical depth of aerosols in the near-IR using a Monte Carlo approach: Application to the OMEGA observations of high-latitude regions of Mars. *Journal of Geophysical Research* 112:E08S13.
Viviano-Beck C. E., Seelos F. P., Murchie S. L., Kahn E. G., Seelos K. D., Taylor H. W., Taylor K., Ehlmann B. L., Wiseman S. M., Mustard J. F., and Morgan M. F. 2014. Revised CRISM spectral parameters and summary products based on the currently detected mineral diversity on Mars. *Journal of Geophysical Research: Planets* 119:1403–1431.
Yingst R. A., Kah L. C., Palucis M., Williams R. M. E., Garvin J., Bridges J. C., Bridges N., Deen R. G., Farmer J., Gasnault O., Goetz W., Hamilton V. E., Hipkin V., Jensen J. K., King P. L., Koefoed A., Le Mouélic S. P., Madsen M. B., Mangold N., Martinez-Frias J., Maurice S., McCartney E. M., Newsom H., Pariser O., Sautter V. H., and Wiens R. C. 2013. Characteristics of pebble- and cobble-sized clasts along the Curiosity rover traverse from Bradbury Landing to Rocknest. *Journal of Geophysical Research: Planets* 118:2361–2380.
Xirouchakis D., Draper D. S., Schwandt C. S., and Lanzirotti A. 2002. Crystallization conditions of Los Angeles, a basaltic Martian meteorite. *Geochimica et Cosmochimica Acta* 66:1867–1880.
Yingst R. A., Cropper K., Gupta S., Kah L. C., Williams R. M. E., Blank J., Calef F., Hamilton V. E., Lewis K., Shechet J., McBride M., Bridges N., Frias J. M., and Newsom H. 2016. Characteristics of pebble and cobble-sized clasts along the Curiosity rover traverse from sol 100 to 750: Terrain types, potential sources, and transport mechanisms. *Icarus* 280:72–92.

SUPPORTING INFORMATION

Additional supporting information may be found in the online version of this article:

Fig. S1. Data processing workflow for Hapke unmixing work presented. * Not every test was applied to every spectral data set, see body of paper for details.

Fig. S2. SSA spectra reconstructed from the input CRISM FRT MP89 SSA endmembers and the estimated abundances from the hyperFcls, MLM, and SUnSAL_TV unmixing programs. The original SSA input mixture spectra are shown in black solid lines with the reconstructed spectra in red dashed lines. These represent good visual matches with a range of low value RMSE results. Corresponding abundances and RMSE are shown in Fig. 3.

Fig. S3. Volume abundance estimates from the six unmixing programs applied to the Hapke transformed SSA CRISM MSP MP89 spectra using the three actual endmember spectra resampled to CRISM MSP wavelengths, compared to the actual mineral endmember mass fraction abundance values for each mixture in the MP89 data set. Red = olivine (olv), green = enstatite (enst), blue = anorthite (anor), and squares = olv + enst mixture, asterisks = olv + anor mixture, diamonds = anor + enst mixture, plus signs = ternary mix of olv + enst + anor. Solid, dashed, and dotted lines represent a one-to-one fit, a 5% error, and a 10% error in volume abundance estimation, respectively. Under each abundance plot are the associated RMSE results comparing the input SSA spectra to those reconstructed from the input endmembers and the estimated abundance results from the relevant unmixing program. The *x*-axis represents the 23 spectra in the MP89 data set in the order listed in the caption for Fig. 1 with the symbols again representing the mixture type as in the associated volume abundance plots.

Fig. S4. Volume abundance estimates from the six unmixing programs applied to the Hapke transformed SSA CRISM FRT MP89 spectra with additional 35dB of Poisson white noise using the three actual endmember spectra, compared to the actual mineral endmember volume abundance values for each mixture in the MP89 data set. Red = olivine (olv), green = enstatite (enst), blue = anorthite (anor), and squares = olv + enst mixture, asterisks = olv + anor mixture, diamonds = anor + enst mixture, plus signs = ternary mix of olv + enst + anor. Solid, dashed, and dotted lines represent a one-to-one fit, a 5% error, and a 10% error in volume abundance estimation, respectively. Under each abundance plot are the associated RMSE results comparing the input SSA spectra to those reconstructed from the input endmembers and the estimated abundance results from the relevant unmixing program. The *x*-axis represents the 23 spectra in the MP89 data set in the order listed in the caption for Fig. 1 with the symbols again representing the mixture type as in the associated volume abundance plots.

Fig. S5. Volume abundance estimates from the five unmixing programs using the Hapke transformed SSA CRISM FRT MP89 spectra and the RELAB mafic endmember library minus the three actual endmember spectra, compared to the mineral endmember volume abundance values for each spectra in the MP89 data set. Red = olivine (olv), green = enstatite (enst), blue = anorthite (anor), and squares = olv + enst mixture, asterisks = olv + anor mixture, diamonds = anor + enst mixture, plus signs = ternary mix of olv + enst + anor. Solid, dashed, and dotted lines represent a one-to-one fit, a 5% error, and a 10% error in volume abundance estimation, respectively. Under each abundance plot are the associated RMSE results comparing the input SSA spectra to those reconstructed from the input endmembers and the estimated abundance results from the relevant unmixing program. The *x*-axis represents the 23 spectra in the MP89 data set in the order listed in the caption for Fig. 1 with the symbols again representing the mixture type as in the associated volume abundance plots.

Fig. S6. Abundance estimates from the five unmixing programs using the Hapke transformed SSA CRISM FRT MP89 spectra and the RELAB mafic endmember library plus the three actual endmember spectra, compared to the mineral endmember volume abundance values for each spectra in the MP89 data set. Red = olivine (olv), green = enstatite (enst), blue = anorthite (anor), and squares = olv + enst mixture, asterisks = olv + anor mixture, diamonds = anor + enst mixture, plus signs = ternary mix of olv + enst + anor. Solid, dashed, and dotted lines represent a one-to-one fit, a 5% error, and a 10% error in volume abundance estimation, respectively. Under each abundance plot are the associated RMSE results comparing the input SSA spectra to those reconstructed from the input endmembers and the estimated abundance results from the relevant unmixing program. The *x*-axis represents the 23 spectra in the MP89 data set in the order listed in the caption for Fig. 1 with the symbols again representing the mixture type as in the associated volume abundance plots.

Fig. S7. SSA spectra reconstructed from the input CRISM FRT RELAB Mafic 272 endmembers and the estimated abundances from the hyperFcls, MLM, and SUnSAL_TV unmixing programs. The original SSA input mixture spectra are shown in black solid lines with the reconstructed spectra in red dashed lines. Corresponding RMSE values and abundances shown in Fig. S5.

Fig. S8. Volume abundance estimates from three unmixing programs applied to the shergottite spectral data set using the extended RELAB Mafic endmembers library, plotted against the actual bulk mineralogy abundance values taken as the average of the values in Table 1. Blue squares = pyroxene, red diamonds = maskelynite, green asterisks = olivine, and black diamonds = mesostasis. The horizontal error bars represent the spread in the reported bulk mineralogy values in Table 1. Solid, dashed, and dotted lines represent a one-to-one fit, a 5% error, and a 10% error in volume abundance estimation, respectively. Under each abundance plot are the RMSE results comparing the input SSA spectra to those reconstructed from the input endmembers and the estimated abundance results from the relevant unmixing program. The *x*-axis represents the 19 spectra in the shergottite data set in the order listed in the caption for Fig. 2 with the colors representing the meteorite subtype as in Fig. 2 where blues = intermediate ultramafic poikilitic, grays/blacks = intermediate permafic olivine-phyric and mafic, greens = enriched mafic diabasic, reds = depleted mafic diabasic, and yellows = enriched mafic intersertal.